J. Fluid Mech. (1992), *vol.* 239, *pp.* 309–340
Printed in Great Britain

The energetics of breaking events in a resonantly forced internal wave field

By JOHN R. TAYLOR
Centre of Water Research, The University of Western Australia, Nedlands,
Western Australia, 6009

(Received 18 December 1990 and in revised form 21 August 1991)

A series of vertical density profiles was taken in a stratified tank in which a standing internal wave was forced to amplitudes at which it became unstable and, as a result of the instability, localized patches of mixing were generated within the fluid. By re-sorting the density profiles the available potential energy in the patches could be calculated and, by comparison with the average buoyancy flux in the tank (determined from density profiles taken before and after each mixing run), an average efficiency of utilization of available potential energy, η_{APE}, was calculated. Along with previous measurements of the flux Richardson number, Ri_{f}, η_{APE} was used to show that the mean value of the overturn Froude number, Fr_{t}, in the patches was 1, thus implying a balance between the rate of release of available potential energy and dissipation in the mixing patches. On the other hand, the patch-averaged overturn Reynolds number, Re_{t}, was so low that, based on the results of previous laboratory experiments on stratified mixing in the wake of a biplanar grid, most of the patches cannot have been actively mixing at the time of sampling.

It is shown that the temperature and conductivity gradient spectra in different patches can be interpreted in a way consistent with the visualization of mixing events, that is, showing an evolution from the generation of an initially unstable density distribution, through the formation of coherent structures as the fluid restratifies and finally the degeneration of these structures into the finer scales of motion at which mixing occurs.

1. Introduction

Breaking internal waves are thought to generate much of the background turbulence and hence diapycnal mixing in the interior of the ocean and atmosphere (Gregg 1989; Fritts 1989). In this paper we report the results of a laboratory experiment in which a standing internal gravity wave was forced to large amplitude and the forcing maintained so that the motion in the tank was driven by the forced wave, parasitic wave modes and small-scale instabilities and mixing events. The nature of the wave breaking events was investigated using flow visualization and vertical profiles taken with conductivity and thermistor probes. Using the density profiles from these measurements, typical lengthscales and buoyancy anomalies within the overturning patches were evaluated. These quantities were used to calculate the amount of potential energy available in the overturns and, by comparison with the average buoyancy flux in the tank (determined from density profiles taken before and after each mixing run), the utilization of this available potential energy in mixing. Along with previous measurements of the flux Richardson number the utilization of available potential energy provides a route to evaluate the mean overturn Froude and Reynolds numbers (described below) in the mixing patches.

McEwan (1983*b*) first performed experiments on the mixing generated by the instability of resonantly forced standing internal waves. In his experiments a fundamental-mode internal wave in a linear density stratification was forced by the oscillation of a plate wavemaker hinged about its central horizontal axis. Breaking began soon after the forced wave amplitude exceeded the critical amplitude for the growth of other wave modes via weak second-order resonant interaction, and hence was linked to the interaction between the forced wave and the two (or more) wave modes which extracted energy from the forced mode. Measurements of the Richardson number in the wave field showed that the instabilities were not obviously shear driven but occurred in regions where the density stratification was gravitationally unstable and so were 'advective' instabilities (Munk 1981). McEwan (1983*b*) determined the overall flux Richardson number, Ri_f, the fraction of the rate of production of turbulent kinetic energy within the mixing events which appeared, on average, as a positive buoyancy flux and irreversibly increased the potential energy of the stratification. Ri_f may be defined as

$$Ri_f = b/p_{\mathrm{TKE}} \tag{1}$$

where b is the average buoyancy flux and p_{TKE} is the rate of production of turbulent kinetic energy. Both quantities were averaged over the volume of the tank and time of the mixing run. The turbulent production, p_{TKE}, was determined from measurements of the total work done by the forcing on the wavefield less the component of this work which was dissipated in the sidewall boundary layers and internal shear of both the forced and parasitic wave modes. The buoyancy flux was evaluated from the change of the mean potential energy of the stratification during the mixing runs. From eight runs the average Ri_f was 0.26, with sample standard deviation of 0.06. Note that even though McEwan (1983*b*) called his η a mixing efficiency his definition corresponds to the usual one of Ri_f, while the mixing efficiency is usually defined as $\eta = Ri_f/(1-Ri_f)$ and relates the buoyancy flux to the dissipation of turbulent kinetic energy, ϵ (Osborn 1980):

$$\eta = b/\epsilon. \tag{2}$$

The simple relationship between Ri_f and η follows from writing the turbulent kinetic energy equation, averaged over the volume and duration of many mixing events, as $p_{\mathrm{TKE}} = b+\epsilon$. Experimental measurements of local values of Ri_f for grid-generated turbulence in stratified air (Lienhard & Van Atta 1990) and water tunnels (Stillinger, Helland & Van Atta 1983; Itsweire, Helland & Van Atta 1986; Rohr *et al.* 1988) and overall values for a grid falling through a stratified water column (Linden 1980) show that Ri_f is not constant but varies depending on the relative importance of buoyancy forces to the flow. Using data from the stratified air and water tunnels Ivey & Imberger (1991) suggested that the value of Ri_f depends on the properties of the turbulence which they suggested could be described by the overturn Froude number,

$$Fr_t = \frac{u}{(g'l_d)^{\frac{1}{2}}}, \tag{3}$$

and the overturn Reynolds number,

$$Re_t = \frac{ul_d}{\nu}, \tag{4}$$

where u, g' are the r.m.s. velocity and buoyancy scales and l_{d} is the observed overturning scale (Thorpe 1977), which has been argued as being representative of the vertical integralscale of the turbulence (Ivey & Imberger 1991; Imberger & Ivey 1991). The r.m.s. velocity scale, u, is defined by $u = (2u'^2 + w'^2)^{\frac{1}{2}}$, where u' and w' are the r.m.s. horizontal and vertical velocity scales. Fr_{t} is a measure of the relative magnitudes of the inertial and buoyancy forces in an overturn event, while Re_{t} is the ratio of the inertial and viscous forces. Gargett (1988) argues that the appropriate Reynolds number to describe turbulence in a density-stratified environment is $Re_w = w'l_{\mathrm{d}}/\nu$, where w' is the r.m.s. vertical velocity (and l_{d} has been substituted for her lengthscale, h), since the definition of Re_{t} above includes the horizontal velocity scale, u', and the vertical lengthscale, l_{d}. If density stratification imposes substantial anisotropy between the vertical and horizontal ($l_{\mathrm{d}} \ll l_{\mathrm{h}}$, where l_{h} is a horizontal lengthscale) and vertical motions are strongly suppressed relative to the horizontal, then Re_w can be much smaller than Re_{t} (from continuity $Re_w \sim (l_{\mathrm{d}}/l_{\mathrm{h}})Re_{\mathrm{t}}$ or $Re_w \sim (w'/u')Re_{\mathrm{t}}$). On the other hand, available experimental evidence, both for the lengthscale ratio (Itsweire 1984) and velocity scale ratio (Itsweire *et al.* 1986), does not show strong isotropy, although the interpretation of the laboratory data has been the subject of disagreement (Gargett 1988, 1990; Van Atta 1990). Given the lack of conclusive evidence Re_{t} may be taken to be the overturn Reynolds number under the assumption that the energy-containing scales of the turbulence are isotropic; at worst it is an upper limit to the true Reynolds number.

In the experiments of Stillinger *et al.* (1983), Itsweire *et al.* (1986), Rohr *et al.* (1988) and Lienhard & Van Atta (1990) Ri_{f} was determined locally from direct measurements of the turbulent density flux (from the correlation between the fluctuating density and the vertical component of velocity) and the dissipation of turbulent kinetic energy (estimated from measurements of two components of the rate-of-strain tensor) rather than from an overall energy budget. In salt-stratified water Imberger & Ivey (1991) suggest that the maximum Ri_{f} (at $Fr_{\mathrm{t}} = 1$) is around 0.20, somewhat lower than the average in the internal wave breaking experiments of McEwan (1983*b*). However, the experimental data they referenced shows Ri_{f} up to 0.24.

The determination of mixing efficiency has received considerable attention because it has been more feasible to infer diapycnal transport in the ocean and other stratified waters from measurements of dissipation scale parameters such as ϵ, using an assumed value of Ri_{f}, rather than make direct estimates of the fluxes using correlation techniques. Even if the correlation between w' and T' is known from a vertical profile there remains the problem of extracting the appropriately averaged flux from a 'snapshot' through an event (Moum 1989).

From the experiments described above it appears that the average mixing efficiency calculated by McEwan (1983*b*) is very similar to the maximum mixing efficiency in the grid mixing experiments. If, in fact, the efficiency of mechanically driven mixing in a stratified fluid is only a function of the overturn parameters Fr_{t} and Re_{t}, as suggested by Ivey & Imberger (1991), then the mixing events in the interval wave breaking experiment are constrained to have Fr_{t} close to unity and Re_{t} which, for at least some of the time, must be sufficiently high to support a turbulent buoyancy flux. It follows then that internal wave breaking in the interior of the fluid drives the maximum possible diapycnal transport for a given energy input.

2. Scaling

Any density profile through a mixing patch in a stably stratified fluid will show density inversions. If such a profile is re-sorted so that the density increases monotonically with depth (Thorpe 1977) the resulting displacements of individual samples, l, should, with appropriate averaging, be representative of the vertical turbulence lengthscale in the mixing event. This averaged displacement scale is denoted as l_d. Similarly, the buoyancy anomaly, defined by $g_i' = g(\rho_i - \rho_i^{\mathrm{res}})/\rho_0$ where ρ_i^{res} is the density of the ith sample of the resorted profile (Imberger & Ivey 1991), should be an appropriate scale for the buoyancy anomaly in the mixing event after the same averaging operation. Since the re-ordered density profile represents the instantaneous minimum potential energy that the profile would have if all samples were returned reversibly to their equilibrium levels (Dillon 1984) the difference in potential energy between the two states is the available gravitational potential energy per unit mass, (APE) which scales as $g'l_d$.

The inversions in the density profile may be convectively unstable and the timescale for a displaced fluid element to return to its equilibrium level under the influence of buoyancy is

$$t_b \sim (l_d/g')^{\frac{1}{2}}.$$

For an ideal overturn in a linearly stratified fluid, $g' = l_d N^2$ (where $N^2 = -(g/\rho)\overline{\rho_z}$ is the square of the buoyancy frequency and $\overline{\rho_z}$ is the mean vertical density gradient) so that $t_b \sim N^{-1}$. The viscous diffusion timescale for the same fluid element is

$$t_v \sim l_d^2/\nu.$$

The timescales t_b and t_v are equal (and hence viscous and buoyancy forces are of the same magnitude) when

$$(Gr)^{\frac{1}{2}} = \left(\frac{g' l_d^3}{\nu^2}\right)^{\frac{1}{2}} \sim 1. \tag{5}$$

Gr then describes the relative sizes of the buoyancy forces, which drive the re-establishment of a stable density stratification (restratification), and viscous diffusion which resists the acceleration of the displaced element. Alternatively, the right-hand side of (5) could be written as $(l_d/(\nu/N)^{\frac{1}{2}})^2$ and it can be seen as the square of the ratio of the observed overturning scale to the scale, $(\nu/N)^{\frac{1}{2}}$ at which McEwan (1983*b*) states 'viscosity inhibits buoyant untangling.' For convenience (as described below) we introduce the overturn Grashof number, Gr_0 which is taken to be the square root of the convential Gr and is defined by

$$Gr_0 = \left(\frac{g' l_d^3}{\nu^2}\right)^{\frac{1}{2}}, \tag{6}$$

or in terms of the buoyancy frequency, N, $Gr_0 = l_d^2 N/\nu$. In a convectively driven flow the buoyancy force must be dominant, hence if Gr_0 is large, implying that the viscous forces are unimportant, buoyancy must be balanced by inertia. A large value of Gr_0 thus implies that nonlinear effects will be important in the evolution of the overturn and should be favourable for the growth of instabilities and hence the finer scales of motion necessary for mixing to occur. Note that a Grashof rather than Rayleigh number is appropriate because the density difference driving the convection is imposed by the scale of the overturn event which generated the initial unstable density distribution (Turner 1979 p. 240). Further, since the Prandtl number (or Schmidt number) is defined for the present salt-stratified experiments as

$Pr = \nu/\kappa_S \gg 1$ (where κ_S is the diffusivity of the stratifying species), the timescale for diffusion of the density anomaly will be long compared to the viscous diffusion timescale. It follows from their definitions that the three parameters introduced thus far, Fr_t, Re_t and Gr_o, are simply related by

$$Re_\mathrm{t} = Fr_\mathrm{t} Gr_\mathrm{o}. \tag{7}$$

As has been discussed by Gargett (1988) and Yamazaki (1990) the evaluation of u', which is required to evaluate Fr_t and Re_t, is problematical in buoyancy-effected turbulence, even when the velocity fluctuations are directly measured, because of the difficulty of separating internal waves and turbulent contributions to the velocity variance. However, in most field experiments only the dissipation-scale temperature or velocity gradients are directly measured and ϵ is estimated from integration of the velocity gradient spectrum or by fitting the temperature gradient spectrum, usually under the assumption that local isotropy is achieved at dissipation scales (conditions under which this assumption are true were studied by Gargett, Osborn & Nasmyth 1984). To estimate Fr_t and Re_t from ϵ it is then assumed that the turbulence is locally steady (so that production balances dissipation) and further that the turbulence is isotropic at the energy-containing scales. Under these assumptions the turbulence can be characterized by single length and velocity scales. It then follows (Tennekes & Lumley 1972) that

$$u = (\epsilon l_\mathrm{d})^{\frac{1}{3}}$$

and with these assumptions Fr_t and Re_t may be written as

$$Fr_\mathrm{t} = \left(\frac{\epsilon}{g'^{\frac{3}{2}} l_\mathrm{d}^{\frac{1}{2}}}\right)^{\frac{1}{3}} \tag{8}$$

and

$$Re_\mathrm{t} = \frac{\epsilon^{\frac{1}{3}} l_\mathrm{d}^{\frac{4}{3}}}{\nu}. \tag{9}$$

In terms of the buoyancy frequency, N, $Fr_\mathrm{t} = (\epsilon/N^3 l_\mathrm{d}^2)^{\frac{1}{3}}$. The rate of release of available potential energy, $\partial\mathrm{APE}/\partial t$, resulting from the tendency of an overturn to restratify, should scale as $\mathrm{APE}/t_\mathrm{b} = g'^{\frac{3}{2}} l_\mathrm{d}^{\frac{1}{2}}$ or $N^3 l_\mathrm{d}^2$. This is the cube of the denominator of (8) and suggests an alternative interpretation of Fr_t as the one-third power of the ratio of the dissipation of turbulent kinetic energy to the buoyancy-driven rate of release of the available potential energy in an overturn (Ivey & Imberger 1991). If, as postulated by McEwan (1983*a*), the wave breaking events are driven by the potential energy in unstable density distributions (so that the mixing patches are convectively driven) then there must be an overall balance, at equilibrium, between the net production of turbulent kinetic energy by buoyancy and its dissipation by viscosity (since the energy lost to vertical mixing is small or, alternatively, the average $Ri_\mathrm{f} \ll 1$). Hence $\partial\mathrm{APE}/\partial t \sim \epsilon$ or $Fr_\mathrm{t} \sim 1$.

The definition of Fr_t in terms of ϵ and N may also be written as $Fr_\mathrm{t} = (l_\mathrm{O}/l_\mathrm{d})^{\frac{2}{3}}$ where $l_\mathrm{O} = (\epsilon/N^3)^{\frac{1}{2}}$ is the Ozmidov scale (Gargett *et al.* 1984 discuss the history of this lengthscale). Dillon (1982) found that $l_\mathrm{O} = 0.8 l_\mathrm{d}$ over nearly three decades of l_O derived from oceanic microstructure data. This relation implies a mean Fr_t of 0.86. Gargett (1988) concluded that the field data of Gargett *et al.* (1984) also had $Fr_\mathrm{t} \sim 1$. The evidence from these field observations then is that $Fr_\mathrm{t} \sim 1$ for much of the turbulence away from the surface layers in the ocean or other stratified waters. Since turbulence in the ocean thermocline is thought to be predominantly shear driven (Kunze, Williams & Briscoe 1990) $Fr_\mathrm{t} \sim 1$ apparently holds regardless of whether the turbulence results from advective or shear-driven instabilities.

3. Experiments

As in McEwan (1983*b*) the degeneration of a resonantly excited standing internal wave was used to generate the wave breaking events for this study. A standing internal wave was forced by means of a plate wavenumber located in the vertical transverse mid-plane of the tank. This configuration is similar to the second of those used by McEwan (1983*b*). The tank was 5900 mm long by 535 mm wide and contained liquid with an approximately linear density stratification, filled using the two-tank method. The working fluid was filtered tap water with common salt as the stratifying agent. The typical mid-depth value of N^2 was 0.2 s^{-2} and depth was 530 mm. There was also a weak temperature gradient in the tank (typically $\bar{T}_z < 1$ °C m^{-1}) but it made little contribution to the density gradient and, as detailed below, except close to the upper and lower boundaries, temperature can be considered to be a passive tracer.

The wave paddle was mounted in an acrylic section mounted in the centre of the tank. It swung in plain Teflon bearings in cutouts in the top and bottom of the Perspex centre section and was driven at its upper edge by a rod coupled, via a spring-displacement-type force transducer, to an arm moving in the same arc as the paddle. This arm was driven through a 25:1 reduction by a stepper motor controlled from a microcomputer. Using this arrangement the paddle could be driven through a sinusoidal oscillation with both the period and amplitude being controlled in a real time. The clearance between the paddle and tank walls was nominally 1 mm.

During the experiment the output from the force transducer and a precision potentiometer coupled to the axis of the drive arm were logged on a microcomputer. Using these quantities the instantaneous power input to the paddle was calculated and displayed in real time. The paddle moment (corrected for the static signal generated by the inclination of the paddle) and paddle angular displacement were output as analog signals and displayed on an *xy* recorder. This display was used to monitor the phase relationship between the forcing and the wave response and small adjustments to the forcing frequency were made to maintain the work input at close to its maximum level.

Profiles of density in the tank during the periods of wave breaking were derived from repeated conductivity profiles and the average tank temperature. The mean density profiles recorded before and after each run were computed from vertical profiles of conductivity and temperature. The conductivity profiles were taken with two PME 4-electrode micro-conductivity cells (Head 1983) mounted on separate traversing mechanisms above the tank. A fast-response thermistor (Thermometrics FP07) was mounted with one of the conductivity probes. The probes were traversed vertically at 0.1 m s^{-1} and both direct and differentiated output from each probe was logged at 100 Hz. Prior to and after each experiment the conductivity probes were calibrated in salt solutions whose density was measured using an Anton-Paar digital density meter. The thermistor was calibrated against a platinum resistance thermometer.

The noise on the temperature and conductivity signals was dominated by bit noise in the 12 bit analog-to-digital converters used to digitize the signals. For conductivity the resolution was 7×10^{-4} S m^{-1} and for temperature 0.012 °C. If $S = f(c, T)$ then a small change in density, $\Delta\rho$ is given by the linearized equation

$$\Delta\rho = \left(\frac{\partial\rho}{\partial S}\right)\left(\frac{\partial S}{\partial c}\right)\Delta c + \left(\frac{\partial\rho}{\partial S}\right)\left(\frac{\partial S}{\partial T}\right)\Delta T - \left(\frac{\partial\rho}{\partial T}\right)\Delta T, \tag{10}$$

Run number	Forcing amplitude (rad)	Forcing velocity (m s^{-1})	Probe positions 1.	2.
1	0.139	4.4×10^{-3}	0.09	0.80
2	0.174	5.4×10^{-3}	0.09	0.80
3	0.210	6.3×10^{-3}	0.09	0.80
4	0.102	4.9×10^{-3}	0.65	0.29
5	0.138	6.5×10^{-3}	0.65	0.29
6	0.172	7.8×10^{-3}	0.65	0.29

TABLE 1. Parameters in the experimental runs: the run number; the amplitude of the paddle oscillation in radians; the forcing velocity defined by $a_n = -4\alpha\omega h/(\pi M)^2$ (where α is amplitude of paddle angular displacement, ω the forcing frequency, h fluid depth and M the vertical mode number, McEwan *et al.* 1972; and the relative locations of the vertical profiles with 0 corresponding to a node in the isopycnal displacement and 1 an antinode.

where S is the salinity and c the specific conductivity. The second term in (10) is the apparent change of salinity due to the effect of temperature on conductivity. The expected density resolution is then

$$\left(\left(\frac{\partial\rho}{\partial S}\frac{\partial S}{\partial c}\Delta c\right)^2+\left(\frac{\partial\rho}{\partial S}\frac{\partial S}{\partial T}\Delta T\right)^2+\left(\frac{\partial\rho}{\partial T}\Delta T\right)^2\right)^{\frac{1}{2}}.$$

Using the derivatives evaluated at the average temperatures and salinity in the experiments the magnitude of the three terms is 3.2×10^{-3}, 1.8×10^{-3} and 2.8×10^{-3} kg m^{-3} respectively. Combining these terms the resolution of the density is 5.0×10^{-3} kg m^{-3}. When re-sorting the density profiles to compute the displacement scale, samples were not interchanged if their densities differed by an amount less than or equal to the calculated density resolution.

As stated above only the conductivity was used in computing the density from profiles made during the breaking periods. This approximation was used, first, because one of the conductivity profilers was mounted without a thermistor and secondly because the thermistor and conductivity probes were separated by approximately 2 mm, and, as will be shown, density fluctuations occur on smaller scales than this. However, the neglect of temperature effects on density is justifiable if temperature was only a passive tracer in the experiments. To show this consider the density perturbation in an overturn, $\Delta\rho' \sim l'\overline{\rho_z}$, where $\overline{\rho_z}$ is the local value of the mean gradient and l' the overturn scale. Expanding as before

$$\Delta\rho = \left(\frac{\partial\rho}{\partial S}\right)\left(\frac{\partial S}{\partial c}\right)l'\overline{c_z}+\left(\frac{\partial\rho}{\partial S}\right)\left(\frac{\partial S}{\partial T}\right)l'\overline{T_z}-\left(\frac{\partial\rho}{\partial T}\right)l'\overline{T_z},$$

where $\overline{c_z}$ and $\overline{T_z}$ are the mean local vertical conductivity and temperature gradients respectively. The second and third terms on the right-hand side are those neglected if the density is calculated from conductivity alone. The minimum vertical scale over which an overturn could be resolved was the sampling interval, 10^{-3} m. With the mean specific conductivity gradient of 3.3 S m^{-2} for a typical series of profiles the magnitude of the conductivity contribution to $\Delta\rho'$ was 1.7×10^{-2} kg m^{-3}, well above the density resolution of 5.0×10^{-3} kg m^{-3}. The largest temperature contribution, based on the r.m.s. temperature gradient of 2.4 °C m^{-1} rather than the mean (to give an upper estimate to the typical magnitude of temperature effects on density), was

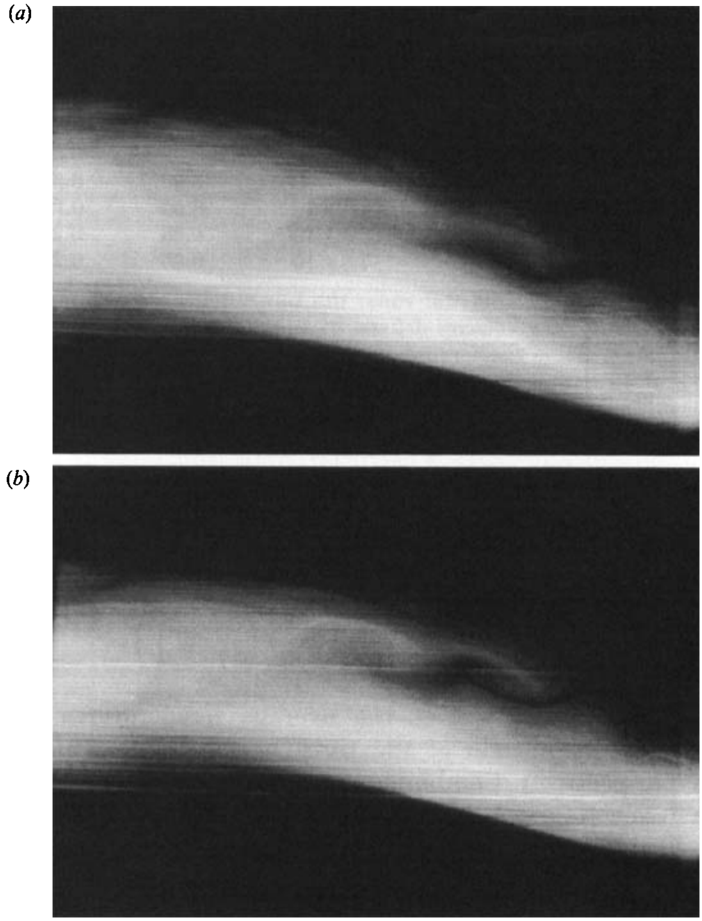

FIGURE 1 (*a*, *b*). For caption see facing page.

only $6 \times 10^{-4}\,\mathrm{kg\,m^{-3}}$, much smaller than the conductivity contribution. Thus, on average, it seems reasonable to neglect temperature effects on density when calculating the density profiles, and temperature can be considered a passive tracer in these experiments.

Both the direct and gradient temperature signals were processed in the spatial domain to compensate for attenuation of the thermistor response using a first-order recursive filter (Fozdar, Parker & Imberger 1985) assuming a 3 dB point in the thermistor response at 120 c.p.m. Given the spatial frequency of sampling, 1000 c.p.m. (giving a Nyquist frequency of 500 c.p.m.), and the anti-aliasing filter 3 dB point at 450 c.p.m., the 3 dB point of the conductivity probe response, at 400 c.p.m. (Head 1983), was at a sufficiently high frequency that no correction for the conductivity probe response was made.

During the filling of the tank a single band of dyed fluid was created at mid-depth by injection of Rhodamine WT dye into the filling line. The mixing events were then visualized by recording the fluorescence of the dye marking the stratification with a CCD video camera. The fluorescence was excited by illuminating the tank from the side with a thin (< 1 mm) vertical light sheet generated by an argon-ion laser. The thickness of the light sheet was minimized by expanding the laser beam and

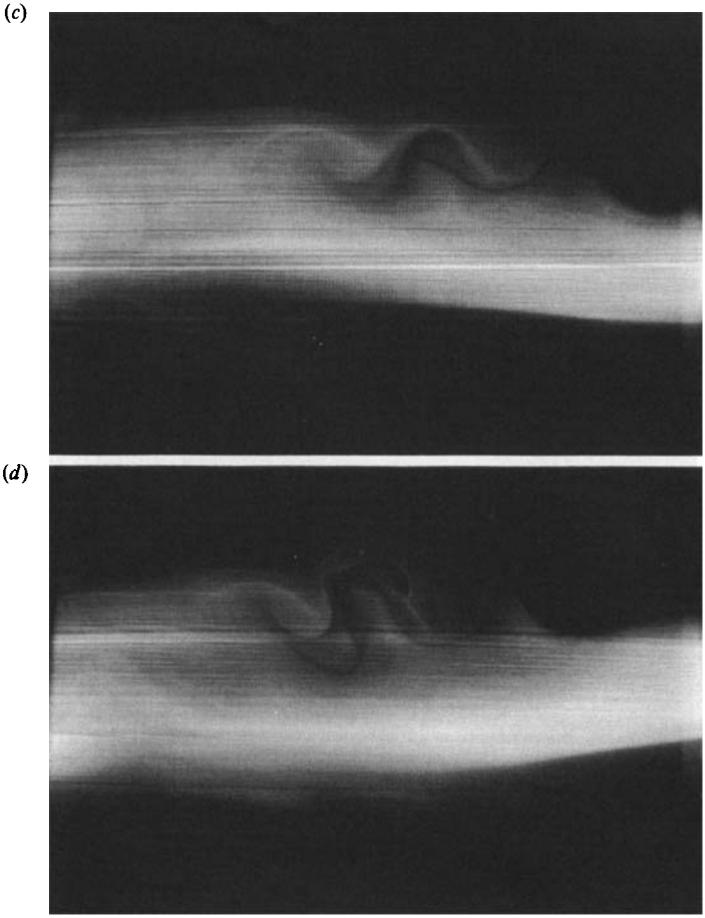

FIGURE 1. Growth of instability on a mode (2, 1) standing wave, run 2. Vertical field of view is 32 cm and the frames are separated by 3.2 s or $1.4N^{-1}$, where N is based on the mid-depth static density profile. The horizontal striations in the images result from refraction of the light sheet by variations in the index of refraction of the fluid to the right of the imaged area.

positioning the waist of the Gaussian laser bean in the region of interest in the tank. Several sequences of images were digitized and stored on disc and the analog video signal was recorded on tape. Because the refractive index was not constant throughout the tank parts of the image were in shadow due to refraction in the mixing events and as a result, the images were only used qualitatively to follow the evolution of the instabilities.

The results to be presented here are from six runs carried out with two fills of the tank (table 1). In the first three runs the forced mode had a (2, 1) structure (two nodes in the horizontal and one in the vertical) and in the second three a mode (3, 1) wave was forced.

4. Results: flow visualization

When the forcing was first turned on the mid-depth dye layer was rather diffuse and remained so as the wave amplitude grew. The first sign of instability was an increasing lumpiness of the dye layer, most likely due to short waves generated by

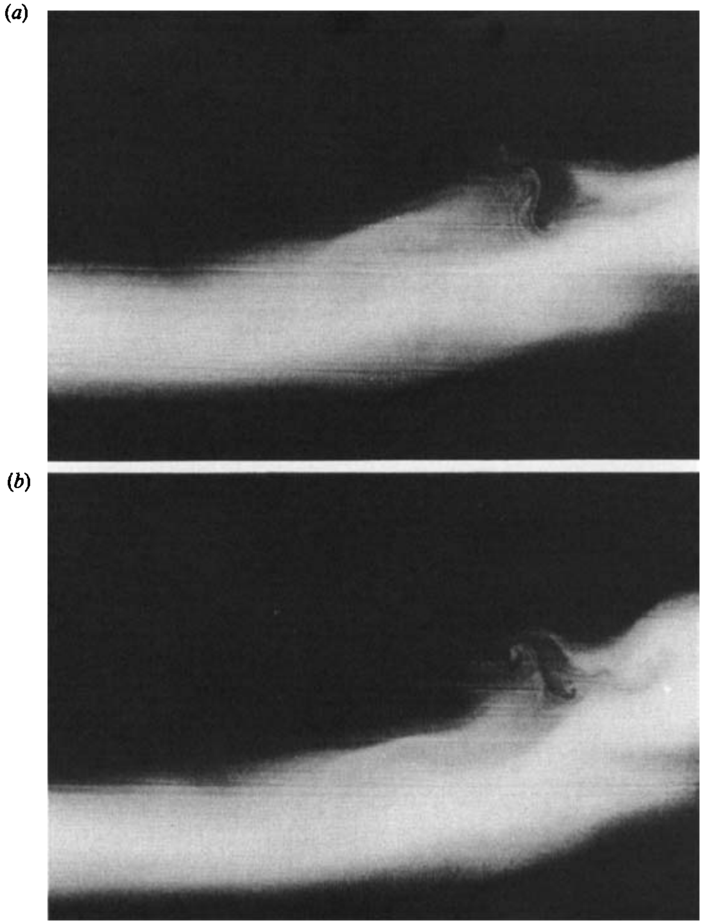

FIGURE 2(*a*, *b*). For caption see facing page.

a parametric instability (McEwan & Robinson 1975). As the amplitude of the forced mode continued to grow the boundaries of the dyed layer became sharp. This sharpening was always a prelude to the formation of local patches of instability and turbulence which appeared first at one location then spread rapidly throughout the tank.

The dye visualization showed a rich array of structures (figures 1 and 2) within mixing events. Using a colour schlieren system calibrated to show the vertical density gradient McEwan (1983*a*) showed that mixing arises in regions where a horizontally elongated statically unstable density gradient is set up by motions driven by the wavefield. Although not calibrated in the same way (since the dye concentration is dynamically unimportant) the present fluorescence images show regions which can also be identified as statically unstable since there is dark (low dye concentration) fluid trapped or entrained below dyed fluid (or vice versa). At the top of the dye layer these regions set up motion reminiscent of a plunging surface breaker, in which a streamer of fluid trapped lighter fluid below. The frequency of occurrence of instabilities changed as the modulation of the forced resonant mode by other, parasitic, wave modes changed. This modulation was most likely associated with changes in the tuning of the forcing as the resonant frequency of the cavity changed.

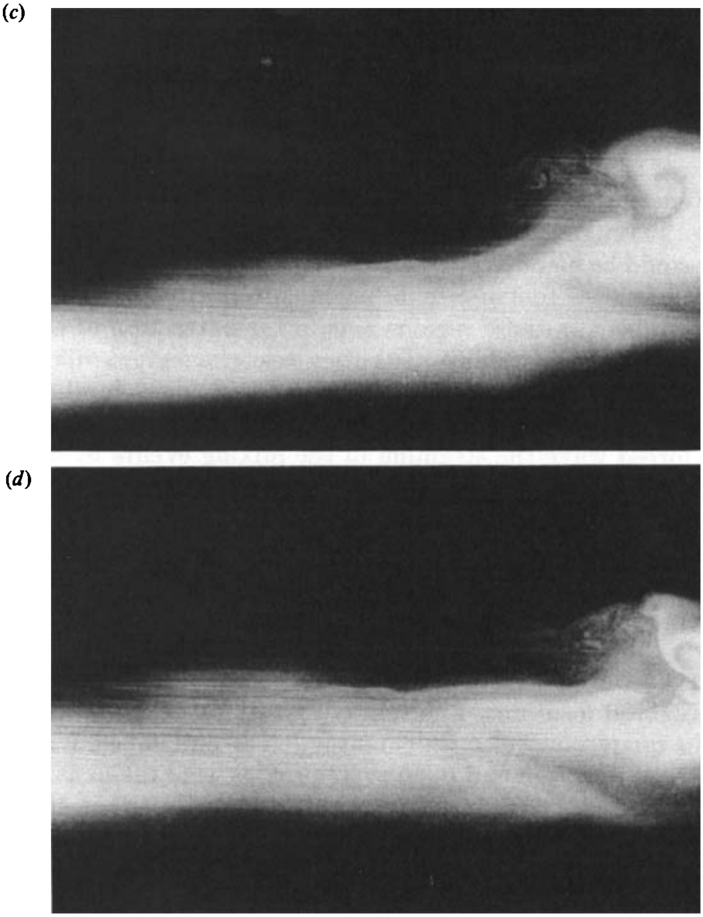

FIGURE 2. Initial instability on a mode (3, 1) standing wave, run 5. Vertical field of view is 32 cm and the frames are separated by 3.2 s or $1.4N^{-1}$, where N is based on the mid-depth static density profile.

One of the striking features in the flow visualization was a structure that resembled a rising thermal (figure 1). These tended to occur in groups along the region of static instability when the background velocity field was divergent, or tended to draw out the region of unstable density gradient, and in appearance resembled Rayleigh–Taylor instability (Tryggvason & Unverdi 1990). In many of the events observed these ordered structures broke down to form a patch of much more random intensity which would be quickly deformed by the unsteady shear in the background velocity field. Occasionally the dye sheet showed an isolated vortex ring, which we identify as a slice through an inclined thermal. The propagation of the vortex rings away from their region of generation confirms the three-dimensionality of the instabilities (Tryggvason & Unverdi 1990).

In other cases the structures were more compressed horizontally and the initial ordered structure which formed resembled more a single roller (figure 2). Often smaller vortices grew parasitically at the boundaries of these regions to generate smaller scales, additional to those generated by the breakdown of the internal density structure of the roller. The appearance of fine scales was generally rapid compared with the time over which the initial instabilities developed. Sometimes the smallest scales appeared as a burst, probably because they were advected into the light sheet.

In general the dye visualization of the breaking waves reinforces the conclusions of McEwan (1983*a*) relating to the results from his schlieren and shear measurements. Most importantly, fine structure in the density and velocity fields generally occurs in regions where there is a static density instability and, as such, it appears that the principle path of energy transfer is from the wavefield to the potential energy of these unstable regions. Through the subsequent gravitational collapse of these regions potential energy could be made available to the smaller scales of motion which strain the local salinity gradients to enhance diffusion. Alternatively, it could be that the positive density gradient in these regions aids in the extraction of energy from the velocity field through shear instability. In either case, the regions of fine gradients do not persist for long and are often strained out by changes in the velocity field associated with the background wavefield. With the background velocity due to the large-amplitude forced wave the straining of the mixing events by the background shear is likely to be at least as important in the horizontal redistribution of the mixed fluid as its gravitationally driven lateral collapse.

5. Results: vertical profiles

5.1. *Processing*

During each run a series of vertical profiles of temperature and conductivity were made at two horizontal locations. The relative positions of the profiles (reduced to the fraction of the quarter-wavelength between a node and antinode) for each run is given in table 1. In runs 3, 4, 5 and 6, 30 or 32 profiles were taken at a time interval of 200 s. Since the average period of the forced modes was either 43 s or 29 s, and much shorter than the time between profiles, any systematic variation of breaking during a wave cycle was not resolved. In runs 1 and 2 bursts of 10 profiles each separated by one wave period were acquired.

Figure 3(*a*) shows a typical density profile taken during a period of breaking. The displacement scale, l (figure 3*c*), calculated by resorting these profiles shows quiet sections (with no resolvable displacements and no zero-crossings in the conductivity gradient, figure 3*b*) and patches of activity. Since the profiles clearly break into sections with and without resolvable displacements, the profiles were simply subdivided on the basis of the displacement scale. In practice, patches were selected by searching the displacement records for sections with greater than a threshold number of consecutive zero-displacement records. Patch boundaries were placed at the edges of these quiet sections. Other methods of segmenting the profiles, based on statistical tests for stationarity in the gradient signals, which have been applied to the interpretation of field microstructure data (Imberger & Ivey 1991), were tested but were of limited use because most of the observed patches were thin relative to the length of the windows needed to compute the criterion on which the tests for stationarity were based.

The mean density profiles had sections at the top and bottom of the record in which the density gradient was weak compared to that at mid-depth. In these sections of the profiles heat was not necessarily a passive tracer and temperature changes induced by evaporation (at the top) and heating (at the bottom) of the profile could introduce displacements in the density profile which were not related to the internal wave breaking; this could be clearly seen if the static profiles were re-sorted in the same way as the profiles taken during the experiments. The re-sorted

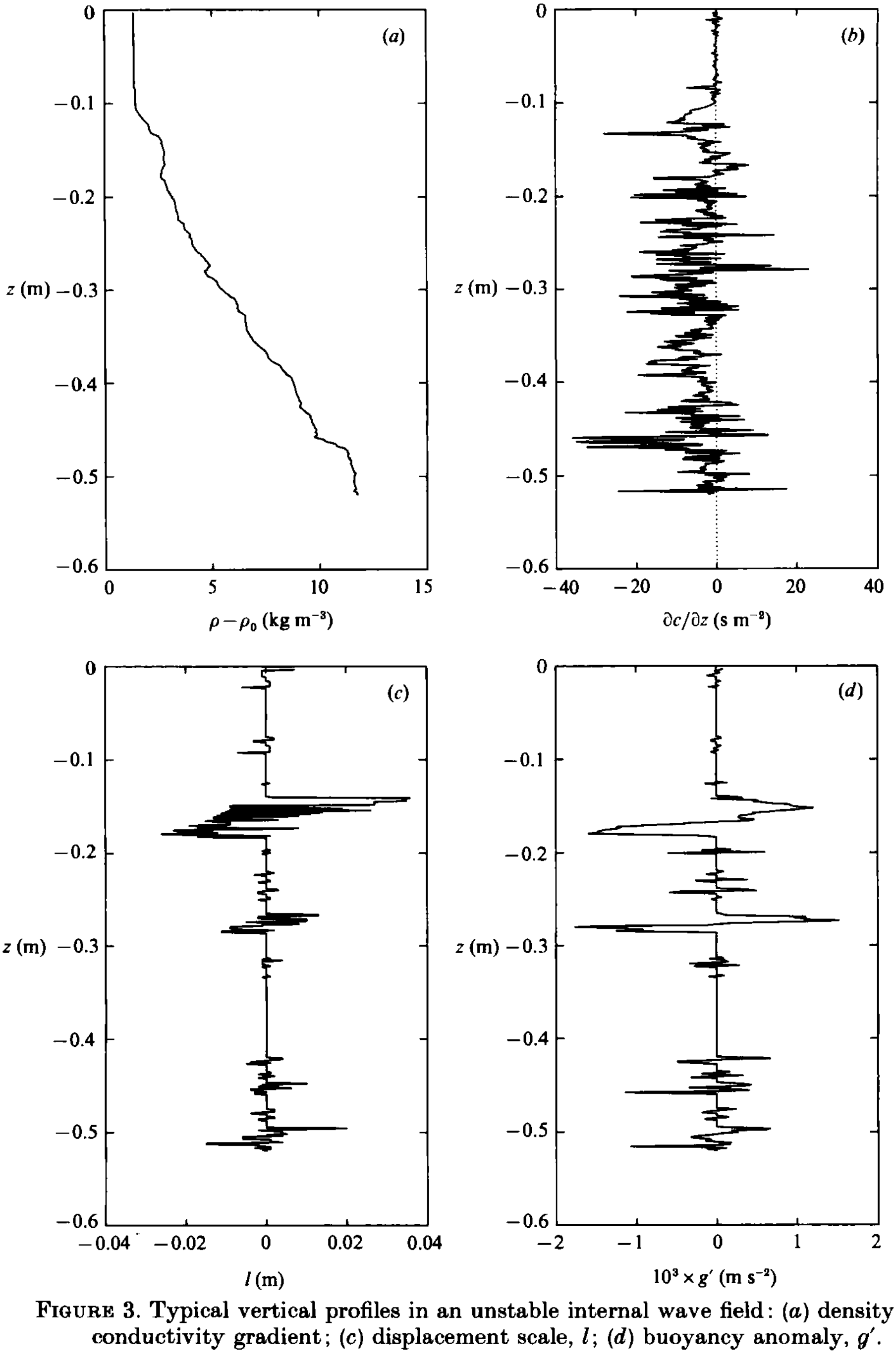

FIGURE 3. Typical vertical profiles in an unstable internal wave field: (*a*) density; (*b*) conductivity gradient; (*c*) displacement scale, l; (*d*) buoyancy anomaly, g'.

static profiles generally had patches with significant thicknesses but only small density anomalies at the top and bottom of the profiles. To ensure that only microstructure patches due to breaking internal waves were included in the following analysis any patch which included either the first or last sample of a profile was excluded.

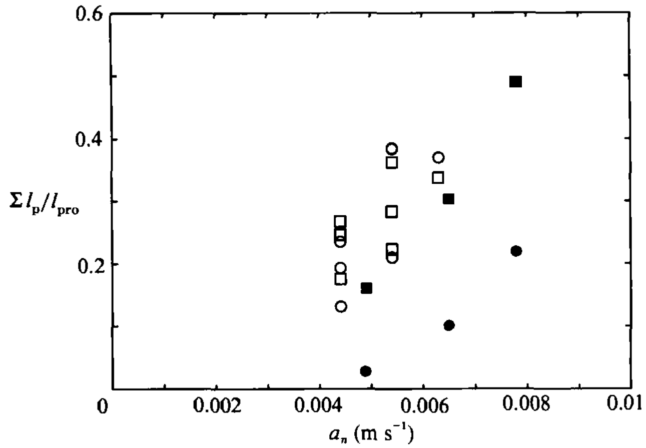

FIGURE 4. Fraction of density profiles containing non-zero displacement lengths as a function of the forcing amplitude for the first vertical mode, $a_n = -4\alpha\omega h/(\pi M)^2$ (see table 1); in the present case $M = 1$. Runs 1, 2 and 3: □, probe position 1; ○, probe position 2. Runs 4, 5 and 6; ■, probe position 1; ●, probe position 2.

5.2. *Overall patch statistics*

The density profiles were first examined to determine the fraction of the profiles that was included in patches (figure 4). In runs 4, 5 and 6 (table 1) this fraction of the profiles clearly increased as the amplitude of the forcing was increased, although the patch fraction was different at the two profiling locations; the profiles taken closer to the antinode had the larger patch fraction. For runs 1, 2 and 3 the patch fraction also increased with increasing forcing amplitude, on average, although there was a large spread in the patch fractions at the two lower amplitudes. This variability reflects the strategy of sampling in bursts of 10 profiles once per cycle with each profile at an approximately fixed phase relative to the forced wave. This method of sampling emphasized both changes in the breaking rate due to drifts in the phase difference between the forcing and resonant mode and the possibility that the amount of breaking might vary strongly during a single wave cycle. In runs 4, 5 and 6 any such changes were averaged out by sampling less frequently over the full period of forcing and at a non-integral multiple of the forced wave frequency.

The trend in the patch fraction with increasing forcing is in keeping with the suggestion of McEwan (1983*a*) that internal mixing occurs 'as a series of widespread but volumetrically small events whose number density is determined by the rate of energisation'. Of course, the observed increase in the fraction of unstable density structure could come about either through there being more events with the same vertical scale (as McEwan suggested), or by larger mixing events occurring at the same number density, and to test this further we need to know more about the characteristics of the events themselves. One point that is clear from the results for the change in patch fraction with forcing amplitude is that the density profiles more widely spaced in time should give a more consistent picture of any change in mixing regime with changes in the forcing so, for the moment, we concentrate on results from runs 4, 5 and 6.

Histograms of the r.m.s. displacement scale, l_d, within the patches were plotted (figure 5) both as raw histograms and probability distributions in which the number of patches in each bin was normalized by the total number of patches for that series of profiles. For all runs the most common r.m.s. displacement was in the bin centred

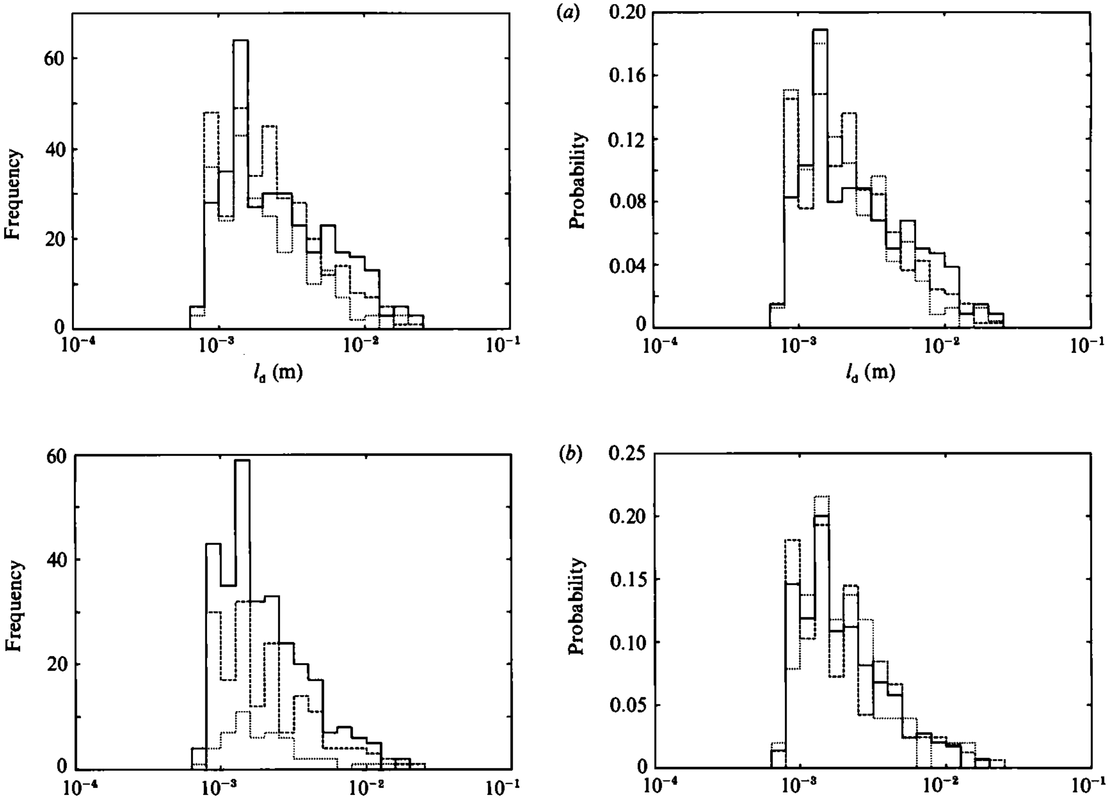

FIGURE 5. Histograms of patch r.m.s. displacement lengths: ....., run 4; ----, run 5; ——, run 6. (*a*) Probe position 1, (*b*) probe position 2. Both raw histograms and probability distributions are shown.

on 1.4×10^{-3} m and the maximum r.m.s. displacement was in the bin centred on 2.2×10^{-2} m. At position 2 the raw histograms for different forcing amplitudes are clearly different, although taking the probability distributions removes much of this dependence on forcing amplitude. At position 1 the change in the raw histogram with changes in the forcing amplitude is less obvious, although the total length of patches (figure 4) at this location did change significantly. There is a trend that intermediate displacement-scale events are more probable with an increase in amplitude at this location. Overall the range of overturning scales changes little as the amplitude of the forcing changes.

The histograms of r.m.s. g' in the patches, plotted in figure 6, shows similar trends to those of l_d. Note that the minimum g' that any particular sample could have is set by the threshold set when re-sorting the density profile, 4.9×10^{-5} m s^{-2}. The frequency or probability of patches drops rapidly once the r.m.s. g' in the patches is less than this value. Essentially, although the frequency of events with a given g' changes with forcing amplitude, taking the probability distributions removes much of the difference, especially at position 2. At position 1 low-g' patches are more probable at the lowest forcing amplitude while intermediate g' is more probable at the largest forcing amplitude. In either case the range of g' values found changes by at most one bin over the range of forcing amplitudes investigated.

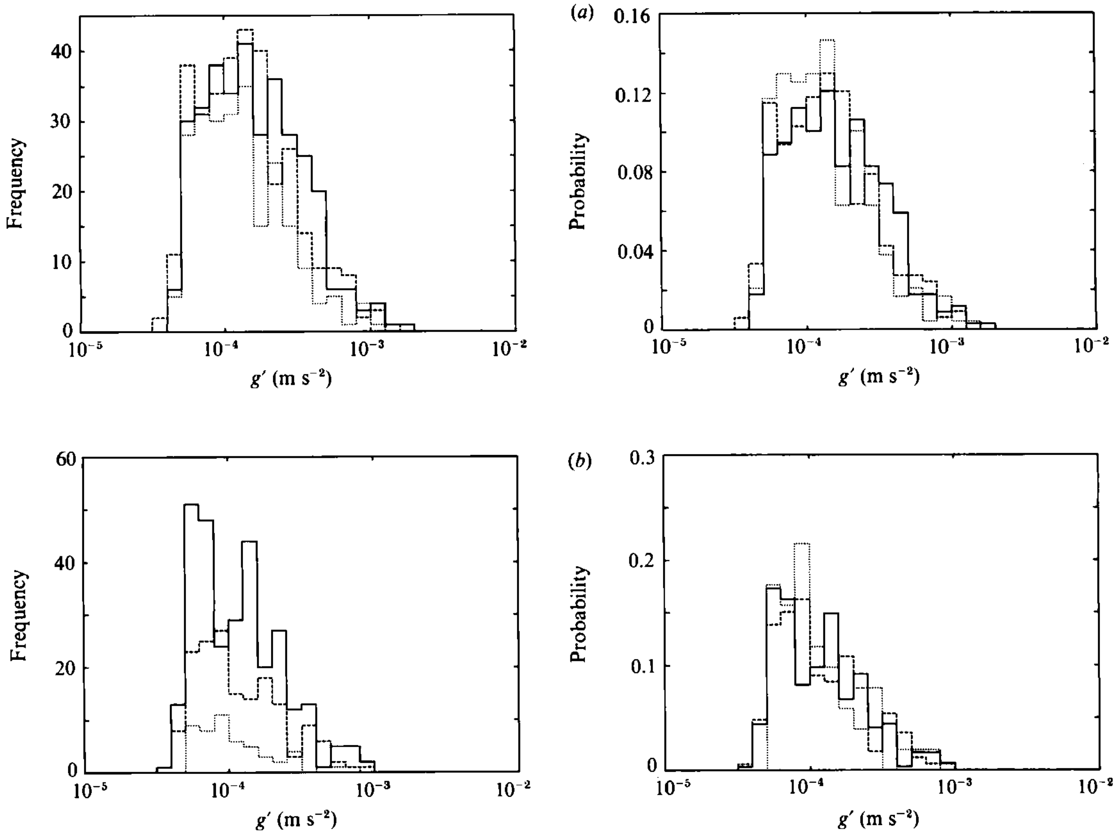

FIGURE 6. Histograms of patch r.m.s. buoyancy anomaly: ....., run 4; ----, run 5; ——, run 6. (*a*) Probe position 1, (*b*) probe position 2. Both raw histograms and probability distributions are shown.

The patch values for l_d and g' were combined to calculate histograms of Gr_0, defined by (5), shown in figure 7. Based on the sample interval and density threshold the minimum Gr_0 should by 0.22 and the amplitude of the histograms drops rapidly for bins with Gr_0 less than this value. In all cases the modal Gr_0 was less than 1. This shows that in the majority of the patches there is insufficient available potential energy in the unstable density distribution to drive a convective flow, so that unless the average $Fr_t \gg 1$ the majority of the patches must contribute little to mixing. As we shall show, the possibility that $Fr_t \gg 1$ is most unlikely based on the overall mixing levels in the tank. As would be expected from the results for l_d and g' from which Gr_0 is derived the range of Gr_0 values changes little as the forcing amplitude is changed, and though the details are a little different at the two locations sampled the probability distributions collapse the results for each forcing amplitude quite well.

In summary, the evidence from the distributions of g', l_d and Gr_0 in the patches is that McEwan's (1983*a*) suggestion that mixing in these wave braking events results from an ensemble of dynamically similar discrete events and that the principal change as more energy is input into the fluid is to increase the frequency of the events is essentially correct. This is best illustrated by the way in which the large difference between the raw histograms for profiles at position 2 in the three different runs was

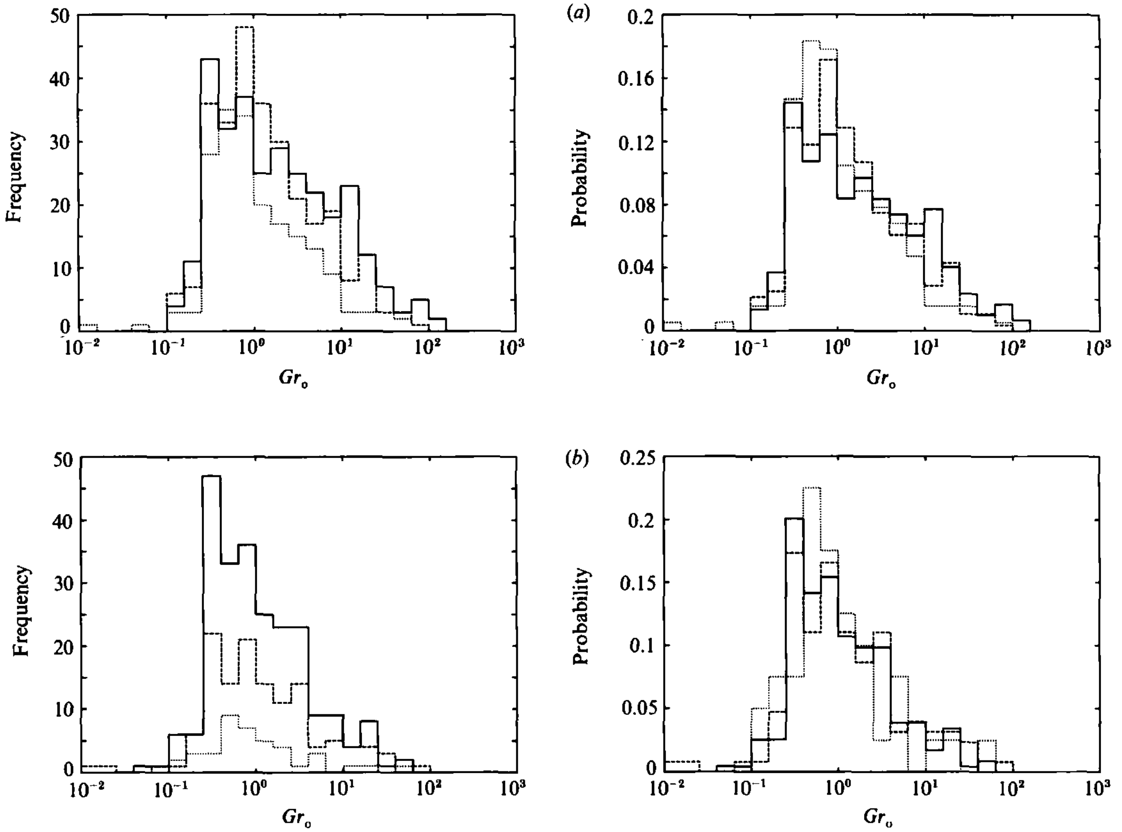

FIGURE 7. Histograms of patch-averaged Gr_0: ....., run 4; ----, run 5; ——, run 6. (*a*) Probe position 1, (*b*) probe position 2. Both raw histograms and probability distributions are shown.

reduced when a probability distribution for each run was calculated. At the same time the range of scales present did not change significantly as the forcing amplitude changed.

5.3. *Overall energetics*

5.3.1. *Utilization of available potential energy*

To determine the net buoyancy flux in the tank during each mixing run a pair of conductivity and temperature profiles was taken before and after each run and the change in the gravitational potential energy between each pair of profiles was calculated. Any drifts in the conductivity probes were compensated for by forcing conservation of salinity in the two sets of profiles. The buoyancy flux, averaged over the total volume of the tank and time of the mixing run, is

$$b = \frac{\Delta \mathrm{PE}}{\rho_0 h t_{\mathrm{m}}},$$

where ΔPE is the measured change in the potential energy of the water column, h is the height of the water column and t_{m} the length of time during which breaking was observed. The average buoyancy flux in the patches is

$$b_{\mathrm{p}} = b\frac{l_{\mathrm{pro}}}{\sum l_{\mathrm{p}}},$$

where l_{pro} is the total length of the water column sampled and $\sum l_{\mathrm{p}}$ the total length of the patches.

Using the mean buoyancy flux in the patches, b_{p}, we can compute an overall average efficiency of utilization of available potential energy, η_{APE}, defined by

$$\eta_{\mathrm{APE}} = \frac{b_{\mathrm{p}}}{\overline{(\partial \mathrm{APE}/\partial t)}}, \tag{11}$$

where

$$\overline{\left(\frac{\partial \mathrm{APE}}{\partial t}\right)} = \frac{\sum (\partial \mathrm{APE}/\partial t)\, l_{\mathrm{p}}}{\sum l_{\mathrm{p}}}.$$

$\partial \mathrm{APE}/\partial t$ is here defined as $g'^{\frac{3}{2}} l_{\mathrm{d}}^{\frac{1}{2}}$ with an equality replacing the scale relationship for this quantity introduced in §2. This is reasonable because $\partial \mathrm{APE}/\partial t$ will only be used as the one-third power of the denominator in the second definition of Fr_{t} (equation (8)). The overbar in (11) denotes both a temporal and spatial average over all the patches in the tank.

Since we only have information from two locations in the tank there is a possibility that $\partial \mathrm{APE}/\partial t$ may have been undersampled owing to the spatial variability of formation of mixing patches. While only a small section of the tank was imaged by the video camera the whole tank could be observed visually and, at least to the eye, there did not appear to be a strong spatial variation in the distribution of mixing events. On the other hand, there was a considerable difference between the way the patch statistics changed at the two locations as the amplitude of the forcing was changed (figure 7) in runs 4, 5 and 6. The best we can do with the present data is assume that the spatial distribution and frequency of the mixing at the sampled locations is a reasonable approximation to that in the whole tank. A comparison can also be made with run 3 where the probes were positioned close to the node and antinode (table 1). Somewhat surprisingly, in this case the fraction of profiles contained in patches (figure 4) at the two sampling locations was very close, compared to those in runs 4, 5, and 6. For runs 1 and 2 when the profiles were taken in short bursts, η_{APE} varied considerably between the groups of profiles. The record of the work input per cycle for these runs showed that relatively high values of η_{APE} were recorded when the work input at the time of the profiles was low, relative to the average for the experiment, and low values of η_{APE} were recorded when the work input at the time of the profiles was relatively high. This would be expected since the buoyancy flux is averaged over the full time of the mixing runs.

Figure 8 shows η_{APE} for runs 3, 4, 5 and 6. For each run a number of calculations of η_{APE} were made, each excluding patches with progressively higher values of Gr_{o}. Each value of η_{APE} on figure 8 was calculated including only patches with Gr_{o} greater than the value given on the horizontal axis. That the efficiency, η_{APE}, is almost constant until all patches with $Gr_{\mathrm{o}} < 2$ are excluded from the calculation shows that such patches contribute little to the average available potential energy, even though, as the histograms show, they make up the bulk of the patches sampled. The values of η_{APE} from runs 4, 5 and 6 increase with increasing forcing amplitude. Since, on the basis of the histograms, we argue that the nature of the mixing events does not change with forcing amplitude, only their frequency, there seems to be no reason why there should be such a variation. In fact, the efficiency for run 3 (which had the largest of the forcing amplitudes for the runs where a (2, 1) mode was forced) is close to the results for run 4. This suggests that the observed variation in η_{APE} may result from undersampling of the distribution of mixing events, and certainly warrants

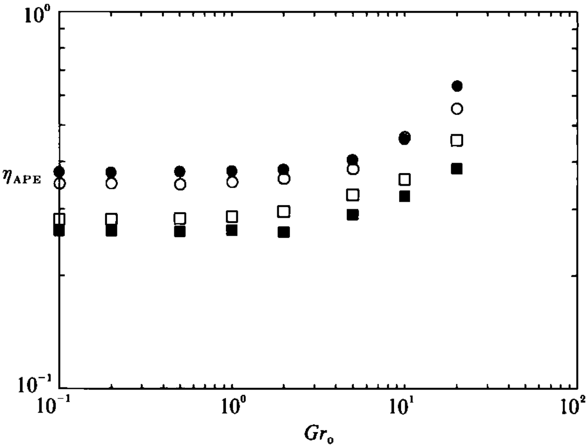

FIGURE 8. The average efficiency of utilization of available potential energy. Each point was calculated including only data from those patches where Gr_0 exceeded the value on the horizontal axis: □, run 3; ■, run 4; ○, run 5; ●, run 6.

further investigation. Given this uncertainty it seems reasonable to define an average η_{APE} for the runs 4, 5, and 6. This average, $\overline{\eta}_{\mathrm{APE}}$, was 0.33.

5.3.2. *Relationship of η_{APE} to Ri_{f} and the average Fr_{t} and Re_{t}*

From the definition of the mixing efficiency η, (2), the efficiency of utilization of APE, (11), and the second form for Fr_{t}, (8), it can be seen that η_{APE} and Ri_{f} are related by Fr_{t} so that

$$Fr_{\mathrm{t}} = \left(\eta_{\mathrm{APE}} \frac{(1-Ri_{\mathrm{f}})}{Ri_{\mathrm{f}}}\right)^{\frac{1}{3}}. \tag{12}$$

Given values for Ri_{f} from previous experimental results and $\overline{\eta}_{\mathrm{APE}}$, an average overturn Froude number for the patches, $\overline{Fr_{\mathrm{t}}}$, was evaluated using (12). Taking $Ri_{\mathrm{f}} = 0.26$, the average flux Richardson number from McEwan (1983*b*), and $\overline{\eta}_{\mathrm{APE}} = 0.33$ gives $\overline{Fr_{\mathrm{t}}} = 1.0$, or 0.9 using $\overline{\eta}_{\mathrm{APE}}$ from run 3. If the lower maximum value of Ri_{f} from the stratified grid mixing experiments (Stillinger *et al.* 1983; Itsweire *et al.* 1986; Rohr *et al.* 1988) suggested by Ivey & Imberger (1991) of 0.2 is used, $\overline{Fr_{\mathrm{t}}} = 1.1$ or 1.0 for run 3. The results for $\overline{Fr_{\mathrm{t}}}$ are in agreement with the expectation that, if the mixing is generated through the collapse of convectively unstable stratifications within the mixing patches, $\overline{Fr_{\mathrm{t}}} \sim 1$. As described previously Dillon (1982) found that the mean Fr_{t} in the ocean thermocline was 0.86. The agreement between the average Fr_{t} in the laboratory and ocean thermocline suggests that the relative importance of buoyancy and inertial forces in mixing events in the two locations is the same.

The average value of Gr_0 for all patches in runs 4, 5 and 6 was 3.7, and 4.7 for run 3 and, since $\overline{Fr_{\mathrm{t}}}$ does not vary significantly from 1, from (7) the mean Re_{t} in the patches is equal to the average Gr_0.

In the stratified grid mixing experiments referenced above, the net buoyancy flux went to zero as the turbulence decayed downstream from the mixing grid when $\epsilon/\nu N^2$ passed through a transition value. With the definition of Fr_{t} and Gr_0 in terms of N a transition Gr_0 can be written:

$$(Gr_0)_{\mathrm{trans}} = \left(\frac{\epsilon}{\nu N^2}\right)_{\mathrm{trans}} \overline{Fr_{\mathrm{t}}}^{-3}.$$

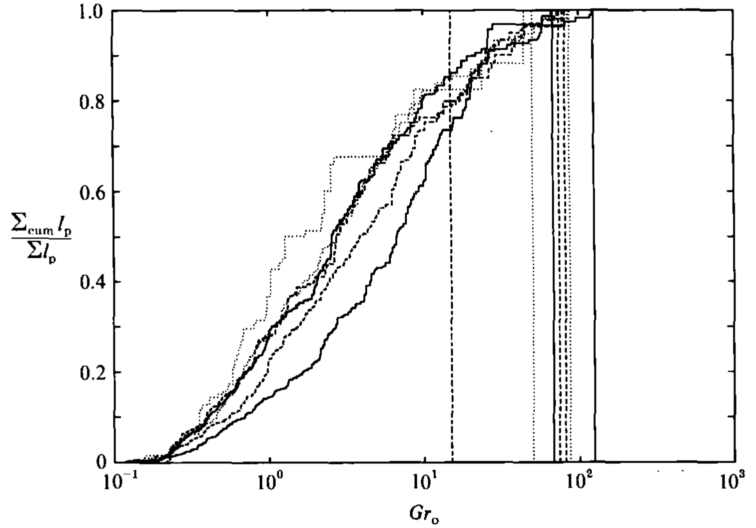

FIGURE 9. Cumulative fraction of the patch length versus Gr_0: ....., run 4; ----, run 5: ——, run 6. The transitional Gr_0 (= 15) is indicated by the double-dash vertical line.

The grid mixing experiments, however, have also shown that the actual value of $\epsilon/\nu N^2$ at this transition varies depending on the geometry of the mixing grid, as well as the Prandtl number of the fluid. While some of the grid mixing experiments also had the same Prandtl number as the present experiments (being salt stratified) the dependence on grid geometry makes the application of the criterion from the grid stirred experiments to the present experiments uncertain. However, even taking the lower limit $(\epsilon/\nu N^2)_{trans}$ from the salt-stratified experiments, shows it is likely that only a small fraction of the patches may have been supporting a buoyancy flux down the mean density gradient at the time of sampling. In fact a plot of the normalized cumulative length of patches plotted as a function of Gr_0 (figure 9) shows that for $(\epsilon/\nu N^2)_{trans} = 15$ (Ivey & Imberger 1991) and with $\overline{Fr_t} = 1$ the fraction of active patches varied from 0.26 to 0.14 of the total length of patches sampled.

5.4. *Temperature and conductivity gradient signals in the patches*

Visualization of the breaking events (§4) showed that they began as ordered overturning structures which subsequently broke down to generate finer scales of motion which would, from their appearance, be classified as turbulence. These finer scales apparently decayed rapidly, although the evidence from the analysis of the overturning and buoyancy scales within the patches was that a significant fraction of the fluid contained small-scale density structure. However, based on the mean Fr_t and Re_t in the tank, the greater fraction of the unstable patches had insufficient available potential to drive a positive buoyancy flux. In the remainder of this section we describe some features of spectra of the temperature and conductivity gradients within several patches and describe how they fit with the observed evolution of mixing events.

Patches greater than 3.2 cm thick (more than 32 samples) were selected for analysis of the temperature and conductivity gradient spectra (32 samples was found to be the minimum length of record from which a reasonable estimate of the spectra could be obtained). Prior to calculating the Fourier transform of the temperature and conductivity gradient signals the linear trend was removed and a Hanning window applied to the data sequences. The raw spectra were band averaged into frequency bands of a geometrically increasing number of points for plotting on log-log axes and 95% confidence levels were calculated based on the number of degrees of freedom being twice the number of points averaged in each band (Chatfield 1984). Temperature and conductivity gradient noise spectra calculated from the central 256 points of profiles taken when the fluid was quiescent before and after the mixing runs. The maximum and minimum values for these quiescent spectra from a number of profiles are plotted with the spectra from each patch. Note that there is some variance from the quiescent profiles at low frequencies in the spectra because of the background temperature and salinity gradients in the tank.

The temperature gradient spectra were compared with the theoretical Batchelor spectrum and the wavenumber of the roll-off in the Batchelor spectrum was used to estimate the dissipation of turbulent kinetic energy within the patch (Dillon & Caldwell 1980; Oakey 1982). The variance of the temperature gradient spectrum defines χ_T, where χ_T is the dissipation of thermal fluctuations (T') defined by (assuming that the temperature gradient is isotropic at dissipation scales)

$$\chi_T = 6\kappa_T \overline{\left(\frac{\partial T'}{\partial z}\right)^2}.$$

The frequency response of the conductivity probes was insufficient to resolve the dissipation peak in the conductivity spectrum. However, in the Appendix we show that, if there is a steady-state balance between production and dissipation, χ_S (the dissipation of salinity fluctuations) and χ_T are simply related by

$$\chi_S = \chi_T(\bar{S}_z/\bar{T}_z)^2, \tag{13}$$

where $\bar{T}_z$ and $\bar{S}_z$ are the patch-averaged vertical temperature and salinity gradients. For the mean S and T gradients of the present experiments, changes in salinity dominated any effects of temperature on the conductivity gradient so that there should be a simple relationship between the conductivity and salinity variance. Thus, when the measured temperature gradient spectrum was fitted, the expected conductivity spectrum was also calculated and compared with that observed.

Figure 10 shows an example of a patch dominated by a large overturn that had little embedded smaller-scale structure (indicated by the lack of zero-crossings in the gradient signal) but a relatively large amount of available potential energy, shown by the value of $Gr_0 = 47$. Such patches were relatively common and, inevitably, Gr_0 for the patch was large. Consistent with the lack of small-scale structure the spectra of temperature and conductivity gradients within this patch both have negative slope. The two spectra are inconsistent with the expected forms of the turbulent dissipation spectra for temperature and conductivity, which shows that there is an imbalance between the potential energy in the unstable density distribution and the turbulent kinetic energy. From this it could be inferred that this patch, and others like it, are in the earliest stage in the development of instability, perhaps corresponding to the formation of the initial region of unstable density gradient observed in the flow visualization. The fact that the largest values of the available potential energy are found in these clean overturns is in accord with the conclusion from flow visualization and suggested previously by McEwan (1983*a*), that most of the mixing is driven by the available potential energy of the overturns. Energy extracted from the mean wavefield goes through this path before some (a relatively small fraction) is finally lost to an increase in the potential energy of the stratification.

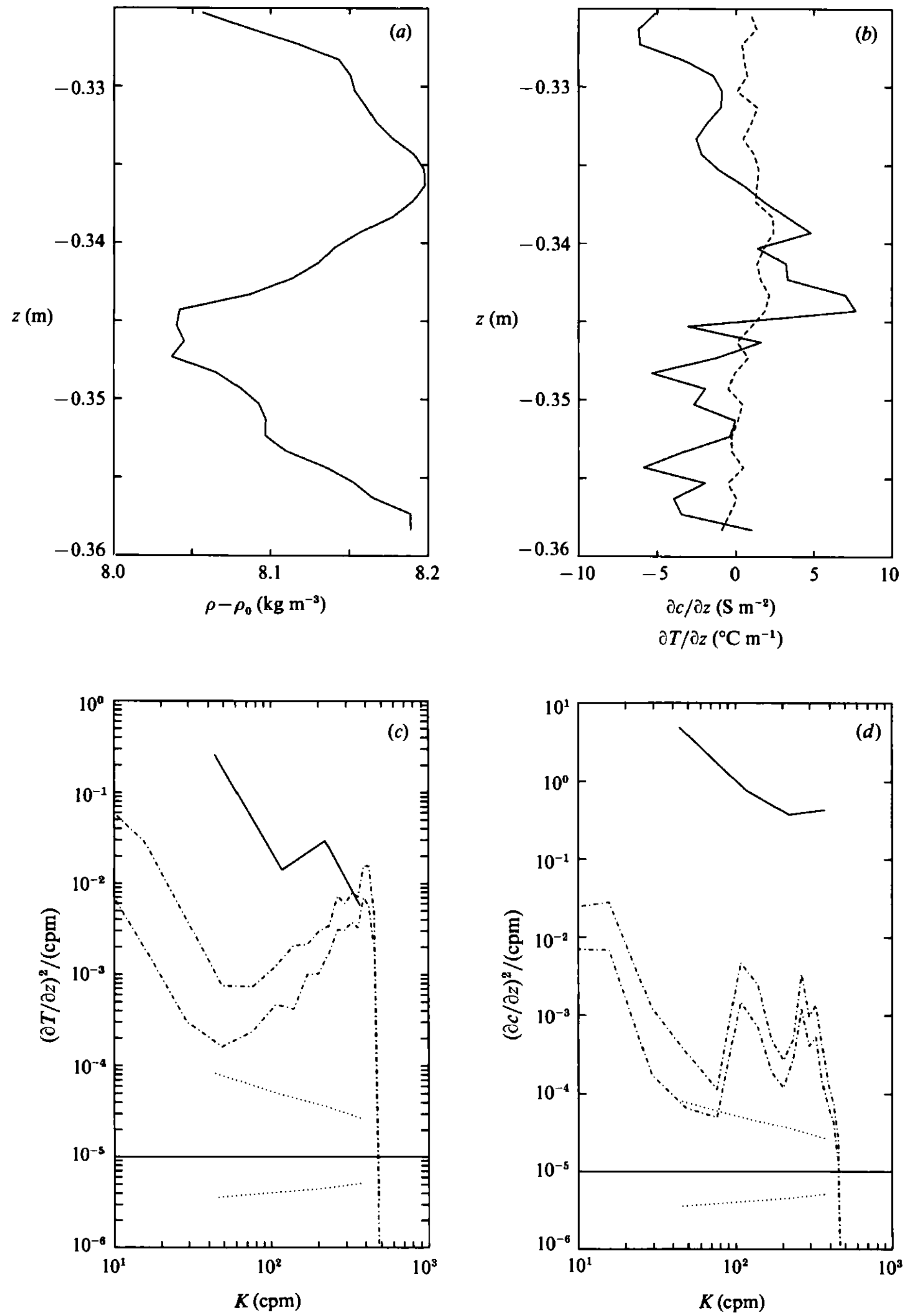

FIGURE 10. Profiles and spectra through patch 34, run 1 containing a relatively large clean overturn. (*a*) density profile; (*b*) conductivity (solid line) and temperature (dashed line) gradients; (*c*) temperature gradient spectrum; (*d*) conductivity gradient spectrum. On the spectrum plots the dash-dot lines are the upper and lower bounds of temperature and conductivity gradient spectra from quiescent profiles and show the noise level. The dotted lines are the 95% confidence limits (Chatfield 1984) plotted relative to the solid horizontal line.

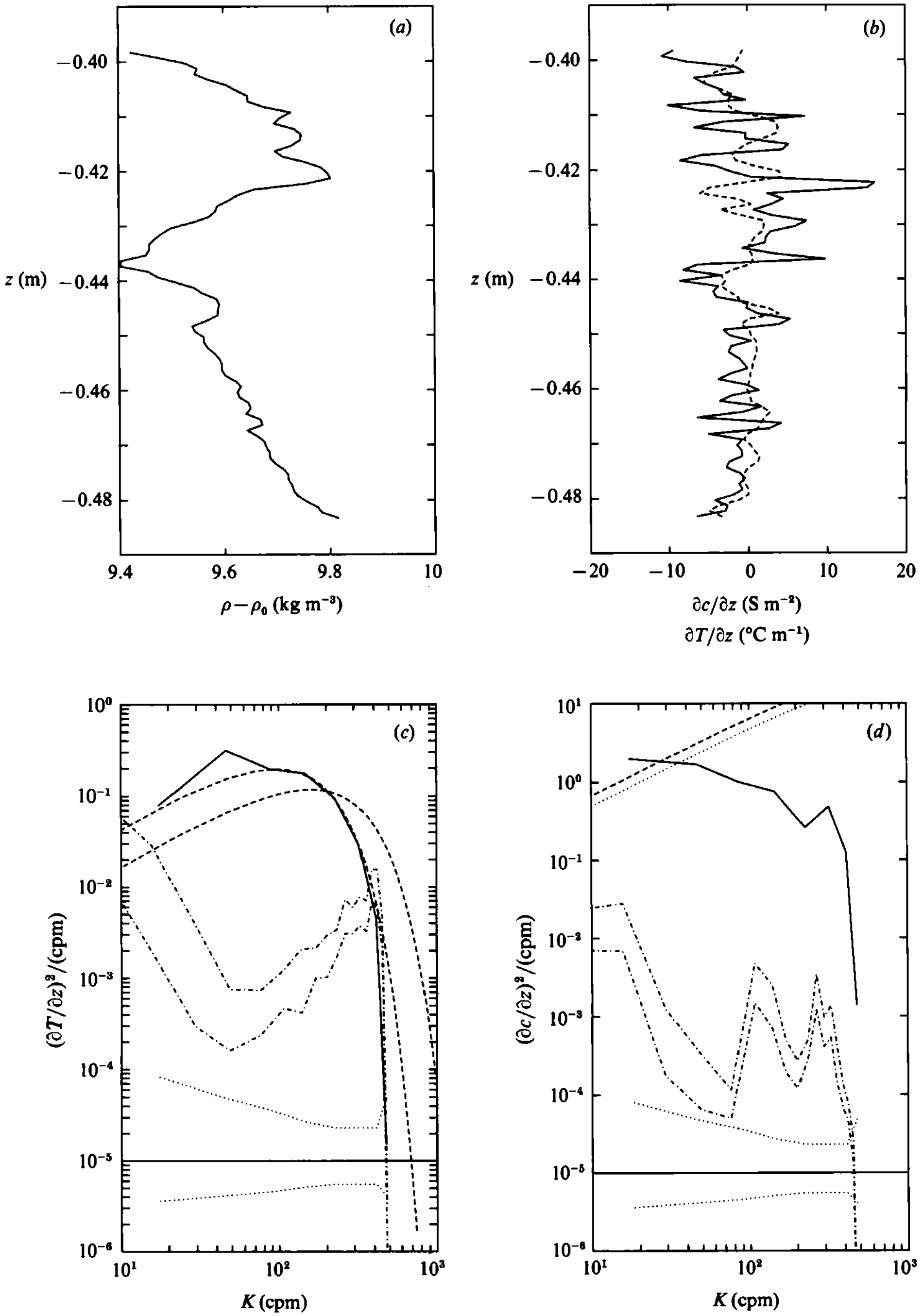

FIGURE 11. Profiles (*a*, density; *b* conductivity) and gradient spectra (*c*, temperature; *d* conductivity) for patch 58, run 1. The dashed lines are Batchelor spectra. The theoretical spectrum which rolls off at the higher wavenumber was calculated assuming $Fr_t = 1$. The Batchelor spectra on the conductivity gradient spectrum plot (*d*) (upper dashed and dotted lines) were calculated using ϵ from the best fit to the temperature gradient spectrum and χ_S from (13). The two curves result from different estimates of $(\bar{S}_z/\bar{T}_z)^2$.

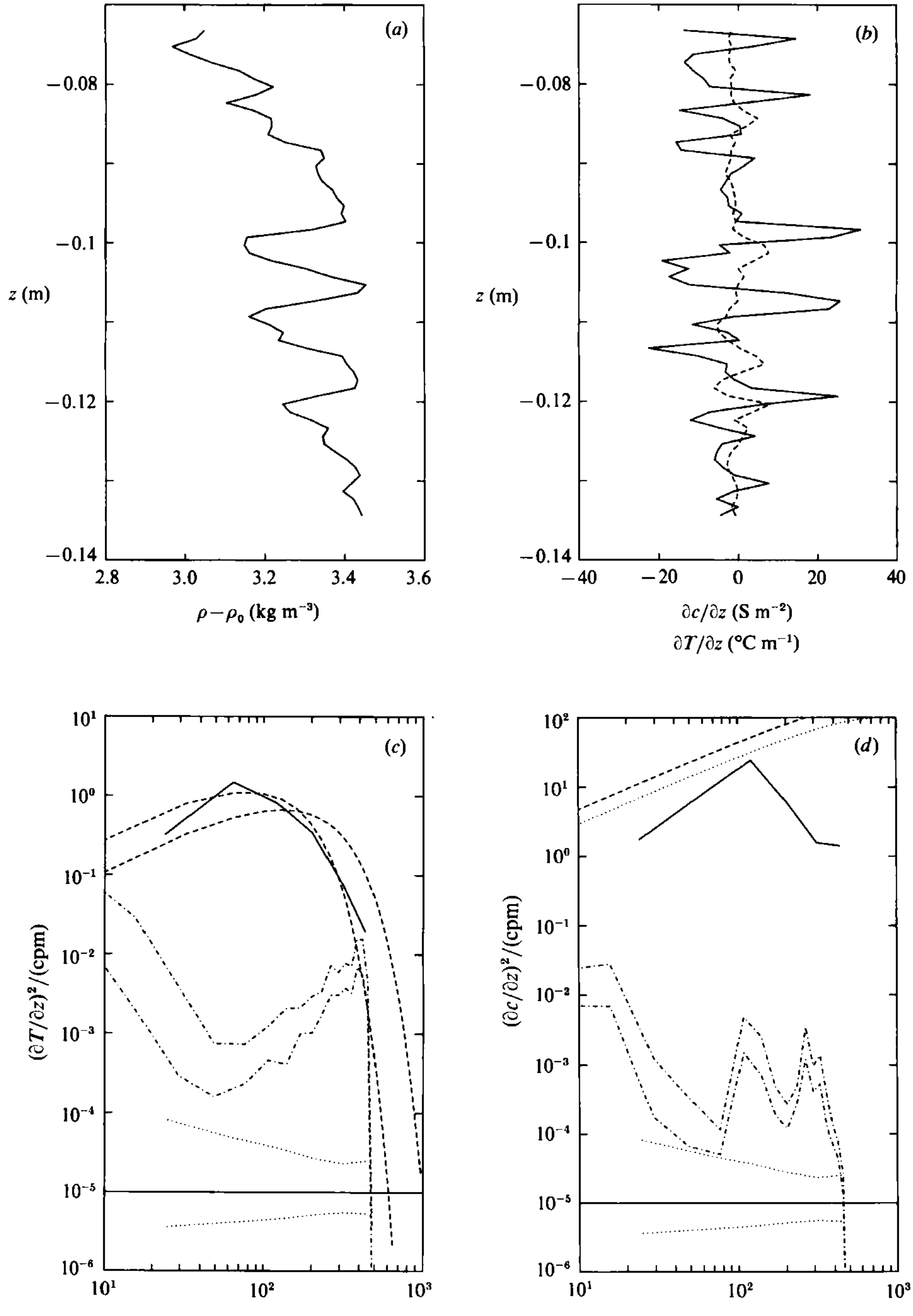

FIGURE 12. Profiles and gradient spectra for patch 208, run 3. Fits to the temperature and conductivity gradient spectrum are as described for figure 11.

As the overturns evolve there should be an increase in the high-frequency content of the gradient spectra. In the spatial domain the large-scale overturns in the density profile become masked by smaller features as the finer scales of motion develop. Figures 11 and 12 show typical examples of such patches, respectively with $Gr_0 = 178$ and $Gr_0 = 50$. For each patch two Batchelor spectra are shown on the plot

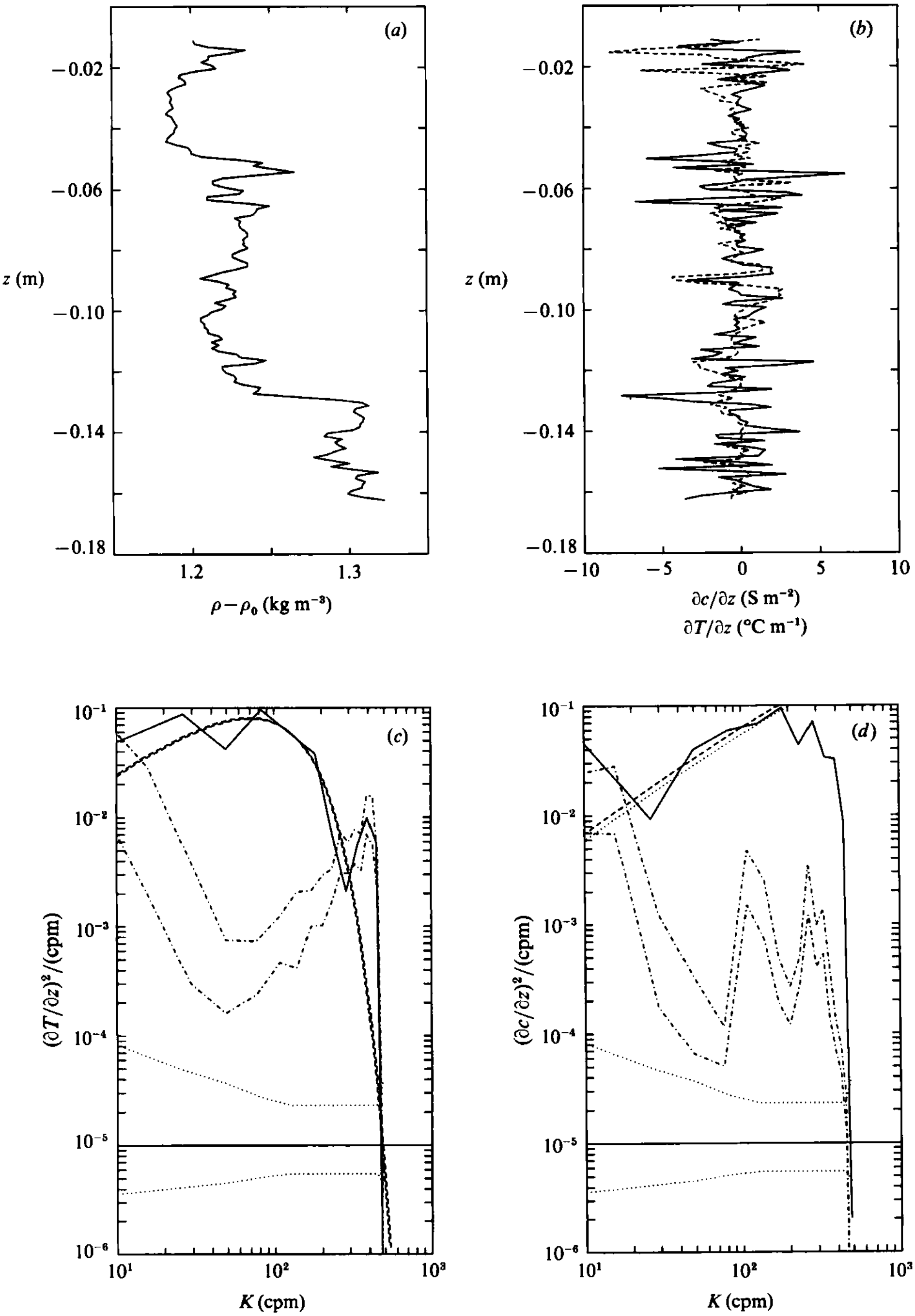

FIGURE 13. Profiles and gradient spectra for patch 49, run 2. Batchelor spectrum calculated with $Fr_t = 1$ (dashed line) gives a good fit to the observed temperature gradient spectrum. Fits to the temperature and conductivity gradient spectrum are as described for figure 11.

of the temperature gradient spectrum, one was calculated assuming that $\epsilon = \partial \mathrm{APE}/\partial t$ or $Fr_t = 1$), the other with ϵ chosen to give the best fit of the theoretical spectrum to the observed spectrum. In both cases the theoretical spectra calculated assuming that $\epsilon = \partial \mathrm{APE}\partial t$ roll off at higher wavenumber than do the measured spectra, so the

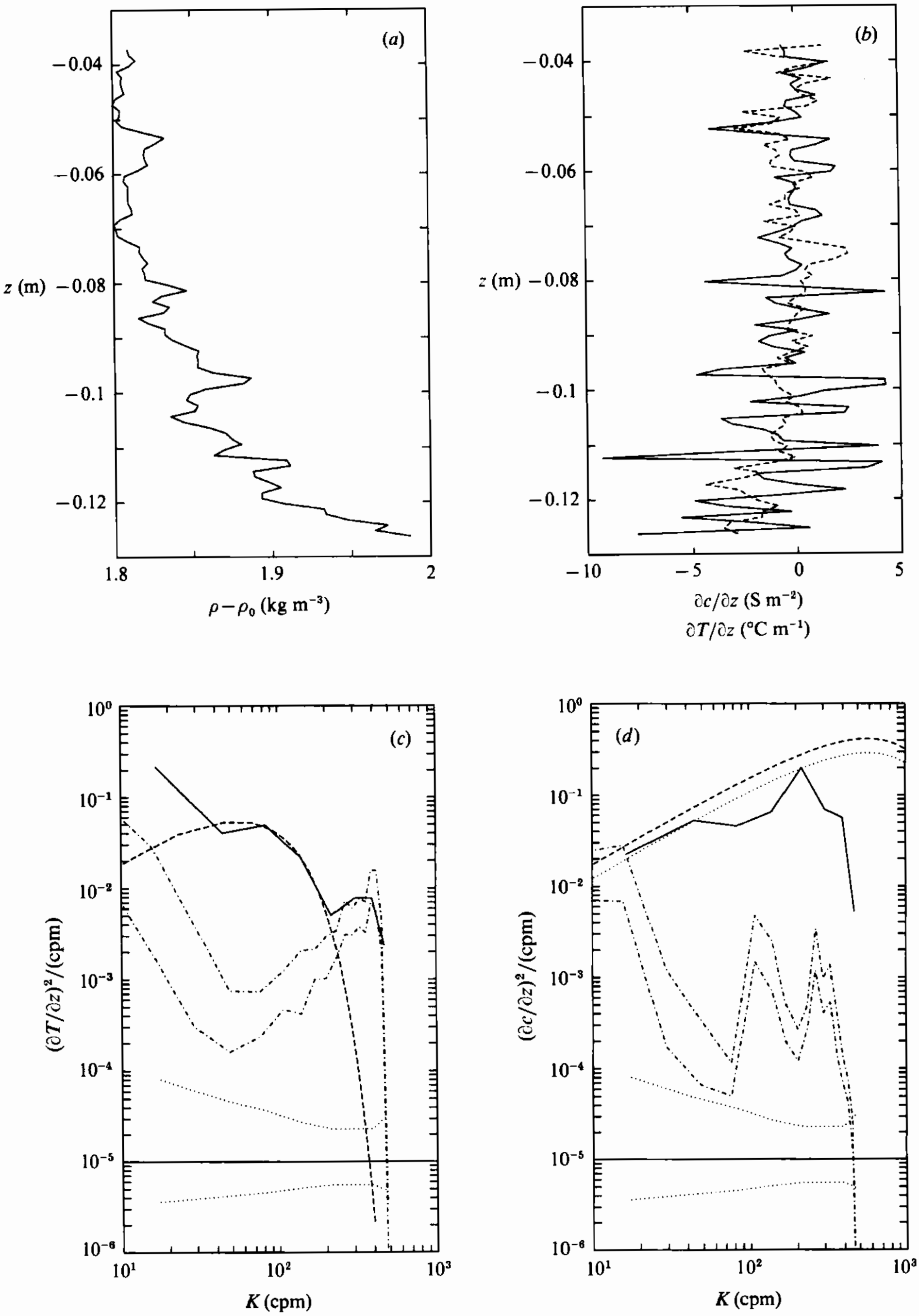

FIGURE 14. Profiles and gradient spectra for patch 39, run 3. Fits to the gradient spectra are as described for figure 13.

rate of release of APE in the patch must have exceeded the dissipation of turbulent kinetic energy at the time of profiling. Thus $Fr_t < 1$. In fact, using ϵ from the best-fit Batchelor spectrum gives $Fr_t = 0.5$ for the two patches and $Re_t = 91$ and 25 respectively. These parameters would put these patches close to the regime where the turbulent buoyancy flux went to zero in the grid mixing experiments, and hence would indicate that turbulence in the patches is decaying. An alternative explanation, in keeping with the large supply of potential energy in these patches, is that they are in the early stages of their turbulent development. If this is the case the turbulent kinetic energy equation would not be expected to be dominated by a simple balance between production and dissipation, so that the parameter Fr_t, as defined by (8), is not likely to be a good description of the balance between inertial and buoyancy forces within the patch. Note that, although the magnitude of the theoretical conductivity dissipation spectra calculated for these two patches using (13) is similar to that of the observed conductivity spectra, the shape of the spectra is not in good agreement. Again this implies a failing in the assumptions of equilibrium between production and dissipation made in deriving the expected relationship between salinity and temperature variance.

Figure 13 shows the density profile and conductivity gradients through a thicker patch made up by many smaller-scale overturns. Both temperature and conductivity gradient spectra are well above noise levels. With the Batchelor spectrum as shown, $Fr_t = 1.0$ and $Re_t = 32$ suggesting that the patch was in a state where dissipation and production of turbulent kinetic energy from the release of available potential energy were close to equilibrium. The conductivity gradient spectrum has a slope and level consistent with the predicted Batchelor spectrum out to a frequency of 200 c.p.m. This patch was one of few which had gradient spectra and hence Fr_t and Re_t consistent with a well-developed, although buoyancy-affected and relatively low-Reynolds-number, turbulent state and should be representative of the active mixing patches in the present experiments. The values of Fr_t and Re_t are within the range of those in mixing patches in the deeper stratified waters of lakes (Imberger & Ivey 1991).

Figure 14 is an example of the most common type of patch which was characterized by small-scale, weak density inversions and small Gr_0, in this case 5.6. The temperature gradient spectrum has a well-defined roll-off region which is consistent with $Fr_t = 1$ which implies that $Re_t = 5.6$, much lower than this would be expected if the patch was turbulent, in the sense of supporting a positive buoyancy flux. There were many similar patches with temperature gradient spectra consistent with $Fr_t \sim 1$ and $Re_t \leqslant 10$. Given the low Fr_t and Re_t in this patch both the temperature and conductivity gradient spectra are surprisingly consistent with the Batchelor form. The presence of high frequencies in both the temperature and conductivity gradient spectra are evidence that this patch is the remnant of a more active mixing event, rather than simply being the result of initially weak overturns.

6. Discussion

At large amplitudes a resonantly forced standing internal wave degenerates, resulting in the formation of patches of instability where there is enhanced vertical transport. For the stratifying species, salt, effective vertical diffusivities averaged over the volume of the tank in the present experiments ranged from 38 to 276 times the molecular diffusivity. Flow visualizations showed that typically, a mixing event started with the creation of a region of static instability. Coherent structures grew in these regions and the degeneration of these structures led to the formation of patches of turbulence. An examination of the density profiles within the patches showed that there was little change in the range of the overturning scales and buoyancy anomalies measured as the amplitude of the forcing increased. Rather, an increase in input energy was accompanied by an increase in the frequency of mixing events and, for some cases, a relatively smaller increase in the probability of occurrence of events with intermediate scales.

McEwan (1983*a*) proposed a model of stratified mixing due to internal wave breaking which was based on the assumption that mixing occurred as a result of discrete, small-volume events in which the principal pathway of energy conversion was from wave energy through the potential energy of the overturns and then into mixing scales. This pathway is in accord with the observed evolution of mixing events in these experiments. In terms of the energetics of the events themselves the pathway implies a balance, over the lifetime of an event, between the release of the available potential energy in the unstable density distribution and the dissipation of turbulent kinetic energy, so that the average $Fr_t \sim 1$. By evaluating the efficiency of utilization of available potential energy it was shown that the average Fr_t in the mixing events was close to 1, in agreement with expectations. Although the fraction of fluid contained within patches with unstable density distributions reached as high as 0.5 of that sampled, the average patch Re_t was only 4, so that most of the patches had insufficient available potential energy to be actively mixing at the time they were sampled. As a result, McEwan's (1983*a*) assumption that the mixing events are small in volume appears to remain valid even at the maximum forcing amplitude in the present experiments.

The spectra of temperature and conductivity gradients within the patches were used to examine the state of microstructure within the patches, and, in several cases, to calculate patch-averaged Fr_t and Re_t. In the earliest stages of an overturn, the spectra of temperature and conductivity gradients had little energy at high wavenumbers so that Fr_t and Re_t (defined in terms of ϵ, equations (8) and (9)) were small but Gr_0 was large. Patches sampled at what was inferred to be a later stage of evolution still had large Gr_0 but had developed high-wavenumber components of the temperature and conductivity spectra. Fr_t and Re_t were close to the condition where the turbulent buoyancy flux in laboratory stratified grid mixing experiments goes to zero, but the large values of Gr_0 in these patches suggest that, rather than decaying, these patches were in a state where the dissipation of turbulent kinetic energy was not in equilibrium with the supply of available potential energy and the turbulence was still developing. Given the average Re_t it is not surprising that few patches were observed in which turbulence was well developed. However, several patches had $Fr_t \sim 1$ and Re_t comparable with that in previous laboratory experiments with stratified grid mixing, and also to that in the deeper stratified waters of a lake. Finally, there were many patches with spectra consistent with $Re_t < 15$ and small Gr_0. These were most likely the remnants of previously active patches. These decayed patches usually had relatively linear background density gradients with small overturns superimposed. This suggests two things. First, the average rate of vertical diffusion in the patch would be still greater than that due to molecular diffusion down the background mean gradient for some time, even though there was no generation of variance due to active straining of the mean gradient. Secondly, since there were few well-mixed layers within patches, in most cases the mixing induced by the initial large overturns must have been incomplete.

The results of the present experiment makes it clear why McEwan (1983*b*) found that the mixing efficiency due to breaking internal waves varied little as the amplitude of the forcing was changed. It is simply that mixing results from an ensemble of discrete events which occur when some local dynamical instability criterion is satisfied and which reach conditions where $Fr_t \sim 1$. So the conditions

Location	$\epsilon/\nu N^2$
Patchex	13.1
Ring82I	763.4
Patchexn	123.4
Drifter	14.8
Tropic heat	2.7
$\kappa_\rho = 1.0\times10^{-4}\ \mathrm{m^2\,s^{-1}}$	400
McEwan (1983*b*) minimum	0.13
McEwan (1983*b*) maximum	5.9
Run 4	0.5
Run 5	1.6
Run 6	2.4

TABLE 2. Comparison of the normalized dissipation levels, $\epsilon/\nu N^2$, from several oceanic locations (Gregg 1989) with those in laboratory experiments. For the entry $\kappa_\rho = 1.0\times10^{-4}\ \mathrm{m^2\,s^{-1}}$ $\epsilon/\nu N^2 = ((1-Ri_f)/Ri_f)(\kappa_\rho/\nu)$ (Osborn 1980), where κ_ρ is the effective diffusivity and it has been assumed that $Ri_f = 0.20$. Note that the values of $\epsilon/\nu N^2$ are averages over the full volume rather than just within mixing patches.

where the maximum mixing efficiency is found in the laboratory experiments with stratified grid mixing are achieved within the mixing events. Changes in the forcing conditions, which McEwan (1983*b*) parameterized in terms of the minimum gradient Richardson number in the background wavefield, should not change the evolution of these discrete events, only their number density. Only in cases where the instabilities do not reach sufficiently high local values of Re_t or the forcing amplitude is so large that mixing is forced directly, rather than through instability of the internal wavefield, would significant changes in Ri_f, or the mixing efficiency, be expected.

Finally, we need to consider whether the dynamics of the mixing in these experiments is similar to that of internal wave breaking observed in natural stratified waters. As has been shown, Fr_t in the two situations is the same. In relation to lakes, as discussed previously, Re_t in mixing patches in the present experiment is comparable with those of some events in the deeper waters of lakes. In the ocean, much more is known about the characteristics of the background wavefield and the levels of associated turbulence. In table 2 we show the normalized mean dissipation levels ($\epsilon/\nu N^2$) at several oceanic locations, compared to those inferred from the present experiments, and also those from McEwan (1983*b*). The most strongly forced laboratory experiments have had $\epsilon/\nu N^2$ a little smaller than that found in the thermocline in the ocean when the energy in the internal wavefield is at the levels of the Garrett and Munk spectrum (Gregg 1989) but up to two orders of magnitude less energetic than the scaled dissipation levels where the internal wavefield is so far above its background levels that it would generate cross-isopycnal diffusivities greater than the canonical vertical diffusivity of $1.0\times10^{-4}\ \mathrm{m^2\,s^{-1}}$. Since $Fr_t \sim 1$ in both the laboratory and field experiments then the average Re_t in the two cases should be similar, at least where the internal wave energy is at, or below, the standard Garrett and Munk spectrum. The only way then that the values of Re_t in the laboratory and oceanic mixing patches could be greatly different is if, even when the internal wavefield is at background energy levels, the overall mixing in the ocean was dominated by a very few extremely energetic events. Available observational evidence (summarized by Gargett 1989) suggests that this is not the case.

The major difference between internal wave breaking in this laboratory experiment and in the ocean is that in the latter case the onset of internal wave breaking events is thought to be primarily due to shear-driven instabilities (Kunze *et al.* 1990) while the laboratory experiments are dominated by instabilities resulting from the overturning of the isopycnals. It has been argued that instabilities of this type, advective instabilities, are dominant in the atmosphere (Fritts 1989).

The comments of J. Imberger, G. N. Ivey and the reviewers of an earlier version of this paper are gratefully acknowledged. This work was supported by the Australian Research Council.

Appendix. Relation between temperature and salinity variance

At equilibrium (and neglecting the advection of variance) the production of temperature and salinity variance by the straining of the mean gradients is balanced by their dissipation (Osborn & Cox 1972) so that the temperature and salinity variance equations reduce to

$$\overline{w'S'}\,\bar{S}_z = 3\kappa_S\overline{\left(\frac{\partial S'}{\partial z}\right)^2}, \quad \overline{w'T'}\,\bar{T}_z = 3\kappa_T\overline{\left(\frac{\partial T'}{\partial z}\right)^2},$$

where isotropy at dissipation scales has been assumed and $\bar{S}_z$ and $\bar{T}_z$ are the mean salinity and temperature gradients. The ratio of the temperature and salinity gradient variances is

$$\frac{\overline{(\partial T'/\partial z)^2}}{\overline{(\partial S'/\partial z)^2}} = \frac{\kappa_S\, c_T\, (\overline{T'^2})^{\frac{1}{2}}\,\bar{T}_z}{\kappa_T\, c_S\, (\overline{S'^2})^{\frac{1}{2}}\,\bar{S}_z},$$

where we have written $\overline{w'S'} = c_S(\overline{S'^2})^{\frac{1}{2}}(\overline{w'^2})^{\frac{1}{2}}$ and $\overline{w'T'} = c_T(\overline{T'^2})^{\frac{1}{2}}(\overline{w'^2})^{\frac{1}{2}}$. $(\overline{S'^2})^{\frac{1}{2}}$ and $(\overline{T'^2})^{\frac{1}{2}}$ are determined by the larger scales of the turbulence, or the product of the r.m.s. displacement scale, l_{d} and mean vertical T and S gradients;

$$(\overline{S'^2})^{\frac{1}{2}} \sim l_{\mathrm{d}}\,\bar{S}_z, \quad (\overline{T'^2})^{\frac{1}{2}} \sim l_{\mathrm{d}}\,\bar{T}_z.$$

Further, assuming that the flux correlation coefficients for temperature and salinity are equal, $c_S = c_T$, then

$$\frac{\overline{(\partial T'/\partial z)^2}}{\overline{(\partial S'/\partial z)^2}} = \frac{\kappa_S}{\kappa_T}\left(\frac{\bar{T}_z}{\bar{S}_z}\right)^2,$$

or in terms of the dissipation of salinity and temperature variance

$$\chi_S = \chi_T(\bar{S}_z/\bar{T}_z)^2.$$

The quantity measured is actually the conductivity gradient and for the conditions of the present experiment

$$\frac{\partial S}{\partial z} \approx \frac{\partial c}{\partial z}\frac{\partial S}{\partial c},$$

where c is the specific conductivity. It follows that the relationship between the expected levels of conductivity gradient and temperature gradient spectra just depends on the ratio of the mean c and T gradients.

REFERENCES

CHATFIELD, C. 1984 *The Analysis of Time Series: An Introduction*. Chapman and Hall. 286 pp.

DILLON, T. M. 1982 Vertical overturns: a comparison of Thorpe and Ozmidov length scales. *J. Geophys. Res.* **87**, 9601–9613.

DILLON, T. M. 1984 The energetics of overturning structures: implications for the theory of fossil turbulence. *J. Phys. Oceanogr.* **14**, 541–549.

Dillon, T. M. & Caldwell, D. R. 1980 The Batchelor spectrum and dissipation in the upper ocean. *J. Geophys. Res.* **85**, 1910–1916.

Fozdar, F. M., Parker, G. J. & Imberger, J. 1985 Matching temperature and conductivity sensor response characteristics. *J. Phys. Oceanogr.* **15**, 1557–1569.

Fritts, D. C. 1989 Gravity wave saturation, turbulence and diffusion in the atmosphere: observation theory and implications. In *Parameterization of Small-Scale Processes, Proc. 'Aha Hulik'a' Hawaiian Winter Workshop* (ed. P. Müller & D. Henderson), pp. 219–234. University of Hawaii at Manoa.

Gargett, A. E. 1988 The scaling of turbulence in the presence of stable stratification. *J. Geophys. Res.* **93**, 5021–5036.

Gargett, A. E. 1989 Ocean turbulence. *Ann. Rev. Fluid Mech.* **21**, 419–451.

Gargett, A. E. 1990 Reply to comments on "the scaling of turbulence in the presence of vertical stratification." *J. Geophys. Res.* **95**, 11675–11677.

Gargett, A. E., Osborn, T. R. & Nasmyth, P. W. 1984 Local isotropy and the decay of turbulence in a stratified fluid. *J. Fluid Mech.* **144**, 231–280.

Gregg, M. C. 1989 Scaling turbulent dissipation in the thermocline. *J. Geophys. Res.* **94**, 9686–9698.

Head, M. J. 1983 The use of miniature four-electrode conductivity probes for high resolution measurement of turbulent density or temperature variations in salt-stratified water flows. Ph.D. dissertation, University of California, San Diego, 211pp.

Imberger, J. & Ivey, G. N. 1991 On the nature of turbulence in a stratified fluid. Part 2: application to lakes. *J. Phys. Oceanogr.* **21**, 659–680.

Itsweire, E. C. 1984 Measurements of vertical overturns in a stably stratified turbulent flow. *Phys. Fluids* **27**, 764–766.

Itsweire, E C., Helland, K. N. & Van Atta, C. W. 1986 The evolution of grid generated turbulence in a stably stratified fluid. *J. Fluid Mech.* **162**, 229–338.

Ivey, G. N. & Imberger, J. 1991 On the nature of turbulence in a stratified fluid, part I: the energetics of mixing. *J. Phys. Oceanogr.* **21**, 650–658.

Kunze, E., Williams, A. J. & Briscoe, M. G. 1990 Observations of shear and vertical stability from a neutrally buoyant float. *J. Geophys. Res.* **95**, 18127–18142.

Lienhard, J. H. & Van Atta, C. W. 1990 The decay of turbulence in thermally stratified flow. *J. Fluid Mech.* **210**, 57–112.

Linden, P. F. 1980 Mixing across a density interface produced by grid turbulence. *J. Fluid Mech.* **100**, 691–703.

McEwan, A. D. 1983*a* The kinematics of stratified mixing through internal wavebreaking. *J. Fluid Mech.* **128**, 47–57.

McEwan, A. D. 1983*b* Internal mixing in stratified fluids. *J. Fluid Mech.* **128**, 59–80.

McEwan, A. D., Mander, D. W. & Smith, R. K. 1972 Forced resonant second-order interaction between damped internal waves. *J. Fluid Mech.* **55**, 589–608.

McEwan, A. D. & Robinson, R. M. 1975 Parametric instability of internal gravity waves. *J. Fluid Mech.* **67**, 667–687.

Moum, J. N. 1989 Measuring turbulent fluxes in the ocean – the quest for κ_ρ. In *Parameterization of Small-Scale Processes, Proc. 'Aha Hulik'a' Hawaiian Winter Workshop* (ed. P. Müller & D. Henderson), pp. 145–156. University of Hawaii at Manoa.

Munk, W. 1981 Internal waves and small-scale processes. In *Evolution of Physical Oceanography* (ed. B. A. Warren & C. Wunsch). The MIT Press, 623pp.

Oakey, N. S. 1982 Determination of the rate of dissipation of turbulent energy from simultaneous temperature and velocity shear microstructure shear measurements. *J. Phys. Oceanogr.* **12**, 256–271.

Osborn, T. R. 1980 Estimates of the local rate of vertical diffusion from dissipation measurements. *J. Phys. Oceanogr.* **10**, 83–89.

Osborn, T. R. & Cox, C. S. 1972 Oceanic fine structure. *Geophys. Fluid. Dyn.* **3**, 321–345.

Rohr, J. J., Itsweire, E. C., Helland, K. N. & Van Atta, C. W. 1988 Growth and decay of turbulence in a stably stratified shear flow. *J. Fluid Mech.* **195**, 77–111.

Stillinger, D. C., Helland, K. N. & Van Atta, C. W. 1983 Experiments on the transition of homogeneous turbulence to internal waves in a stratified fluid. *J. Fluid Mech.* **131**, 91–122.

TENNEKES, H. & LUMLEY, J. L. 1972 *A First Course in Turbulence.* The MIT Press, 300pp.

THORPE, S. A. 1977 Turbulence and mixing in a Scottish loch. *Phil. Trans. R. Soc. Lond.* A**286**, 125–181.

TRYGGVASON, G. & UNVERDI, S. O. 1990 Computations of three-dimensional Rayleigh–Taylor instability. *Phys. Fluids* A**2**, 656–659.

TURNER, J. S. 1979 *Buoyancy Effects in Fluids.* Cambridge University Press, 368pp.

VAN ATTA, C. 1990 Comment on "the scaling of turbulence in the presence of vertical stratification.". *J. Geophys. Res* **95**, 11673–11674.

YAMAZAKI, H. 1990 Stratified turbulence near a critical dissipation rate. *J. Phys. Oceanogr.* **20**, 1583–1598.